Vaz-Romero, A.; Rodríguez-Martínez, J.A.; Arias, A. (2015). The deterministic nature of the fracture location in the dynamic tensile testing of steel sheets. *International Journal of Impact Engineering*. Vol. 86, pp. 318-335.

DOI: https://doi.org/10.1016/j.ijimpeng.2015.08.005

The deterministic nature of the fracture location in the dynamic tensile testing of steel sheets

A. Vaz-Romero*, J. A. Rodríguez-Martínez, A. Arias

Department of Continuum Mechanics and Structural Analysis. University Carlos III of Madrid. Avda. de la Universidad, 30. 28911 Leganés, Madrid, Spain

Abstract

This paper investigates the key mechanisms which determine the fracture location in the dynamic tensile testing of steel sheets. For that purpose we have conducted experiments and finite element simulations. Experiments have been performed using samples with six different gauge lengths, ranging from 20 mm to 140 mm, that have been tested within a wide spectrum of loading velocities, ranging from 1 m/s to 7.5 m/s. Three are the key outcomes derived from the tests: (1) for a given gauge length and applied velocity, the repeatability in the failure location is extremely high, (2) there is a strong interplay between applied velocity, gauge length and fracture location and (3) multiple, and largely regular, localization patterns have been observed in a significant number of the experiments performed using the samples with the shorter gauge lengths. Our experimental findings are explained using the finite element simulations. On the one hand, we have shown that variations in the applied velocity and the gauge length alter the processes of reflection and interaction of waves taking place in the sample during the test, which leads to the systematic motion of the plastic localization along the gauge (as experimentally observed). On the other hand, we have detected that the emergence of multiple localization patterns requires of short and equilibrated specimens with uniform stress and strain distributions along the gauge. We conclude that the experimental and numerical results presented in this paper show that, in absence of significant material and/or geometrical defects, the location of plastic strain localization in the dynamic tensile test is deterministic.

Keywords:

Dynamic tensile experiments, Finite element simulations, Stress waves, Strain localization, Dynamic fracture

*Corresponding author. Tel. +34 916246015; Fax: +34 916249430. E-mail address: avazrome@ing.uc3m.es

1. Introduction

In the decade of the 40's, the pioneering publications of Nadai and Manjoine [1], De Forest et al. [2], Clark [3], Parker and Ferguson [4] and Manjoine [5] represented a significant progress in the research of the dynamic tensile test. These works, motivated by the celebrated papers of Mann [6, 7], definitely showed that high velocity tests are essential to reveal the true dynamic properties of materials. It was recognized that the performance of some materials under dynamic loading is different from that observed under static conditions. For the first time, the effect of velocity on the capacity of metallic materials to absorb energy was demonstrated. Within this context, special mention requires the thorough experimental investigation conducted in the Guggenheim Aeronautical Laboratory of the California Institute of Technology (directed at that time by Theodore Von Kármán) with the aim of evaluating the impact endurance limit of different metals used in aircraft construction [8, 9, 10, 11]. Note that this extensive experimental research was directly driven by industrial concerns. In Beardsley and Coates [9] words *"with the current improvements in aircraft structural design methods, resulting in more efficient structures in which the material is worked at higher stresses, it is becoming increasingly more necessary to consider the effects of dynamic loading on the structure"*.

During the following years, with the continuous support of the aeronautical sector, the efforts were focused on developing a theoretical framework to explain the experimental findings. Thus, Clark and co-workers published a series of papers [12, 13, 14, 15] in which the theory of the elastic and plastic strain propagation developed by Von Kármán and others [16, 17, 18, 19, 20] was used to interpret in a rational manner the experimental data. A key outcome of these theoretical investigations was to show that the strain rate in impact tests varies from point to point along the specimen, and for a given point it is also dependent upon time [14]. This behaviour, which is accentuated as the impact velocity increases, was identified as the main problem of the tension impact test to study the influence of the rate of strain on the properties of metals.

The following decades, especially after the development of the tension version of the Hopkinson-bar technique in the early 60's [21], were very much focused on overcoming this drawback. The belief that the use of very short specimens minimizes the importance of the inertia loads and allows to neglect the intervention of strain propagation phenomena within the specimen became widely accepted [22, 23] and the dynamic stress-strain characteristics of different metallic materials were published, see for instance the works of Nicholas [24, 25, 26]. On the other hand, the works of Lubliner [27] and Botte et al. [28, 29] strengthened the idea that the essential character of the tensile impact test is the non-uniformity in time and space of the state variables of the material. If long specimens are used the parameters which define the state of the material (stress, strain and particle velocity) assume different values in the different sections of the specimen, and they change with time. Botte et al. [28] explicitly stated that numerical analysis becomes indispensable to investigate the spatial-temporal variation of the field variables in detail.

Thus, the advent of computational mechanics gave new impetus to the analysis and understanding of the impact tensile test [30, 31, 32]. The finite element method has been widely used over the last years in the design of tensile specimens suitable to extract the true dynamic properties of metallic materials [33, 34, 35]. Within this context, it has to be highlighted the work of Rusinek et al. [36] who reviewed the performance of six different specimen geometries loaded in impact tension. Driven by the earlier work of Nemes and Eftis [31], Rusinek et al. [36] paid special attention to the interplay between necking inception, impact velocity and specimen geometry. They showed that, as soon as the impact velocity is such that the strain propagation effects become relevant, the necking moves away from the central point of the sample (where it locates under quasi-static conditions). This observation, which agrees with previous experimental results published by Wood [37], suggests that the necking inception in the dynamic tensile test is a deterministic process. Nevertheless, whether the nature of the necking location is deterministic or random is still a controversial issue, as can be seen from the number of recent publications dealing with this precise topic [38, 39, 40].

With the aim of clarifying this controversial issue, in this investigation we have performed an extensive experimental and numerical campaign that reveals the deterministic character of the necking (and fracture) location in the dynamic tensile test. We have carried out dynamic tensile experiments using steel sheet specimens with six different gauge lengths (20 mm, 40 mm, 60 mm, 80 mm, 100 mm and 140 mm) for seven impact velocities (1 m/s, 1.75 m/s, 2.5 m/s, 3.75 m/s, 5 m/s, 6.25 m/s and 7.5 m/s). Similarly to the experiments reported by Wood [37], we have observed that the fracture location moves systematically from side to side of the sample with the variations in impact velocity and gauge length. Further, for each combination of gauge length and applied velocity several repeats are performed which show an extremely high repeatability in the necking (and failure) location. A key, and very unusual, experimental finding of this work is the multiple, and largely regular, localization patterns that have been observed in a significant number of the shortest samples tested. We have explained all these experimental findings with finite element simulations performed in ABAQUS/Explicit [41]. Thus, in agreement with the experiments, the computations have shown that variations in the applied velocity and gauge length lead to the systematic motion of the plastic localization along the gauge. Further, our numerical calculations serve to prove that the emergence of multiple localization patterns is associated to equilibrated specimens with low slenderness ratios and *hardly* subjected to the influence of stress waves.

2. Experimental setup and mechanical characterization

2.1. Material and specimens

The material of this study is annealed AISI 430 stainless steel. Its chemical composition is given in Table 1.

Fe	**C**	**Mn**	**P**	**S**	**Si**	**C**	**Ni**
Balance	0.12 max.	1.00 max.	0.04 max.	0.03 max.	1.00 max.	16.00 - 18.00	0.5 max.

Table 1: *Chemical composition of the AISI 430 stainless steel (wt %) as taken from [42].*

The AISI 430 is one of the most widely used ferritic stainless steels. It shows excellent stress corrosion cracking resistance and good resistance to pitting and crevice corrosion in chlorine environments. Typical consumer product applications include automotive trim and molding and furnace combustion chambers. Industrial and commercial applications range from interior architectural applications to nitric acid plant equipment and oil refinery equipment [42].

The material is supplied in plates of thickness $h = 1$ mm from which tensile specimens are machined. The specimens' geometry and dimensions are shown in Fig. 1. The impacted side is the left side of the specimen in the figure (and therefore the clamped side is the right side). L_0, L_1, L_2, L_3, W and R denote respectively the overall length of the sample, the length of the grip section of the clamped side, the length of the gauge, the length of the grip section of the impacted side, the width of the gauge and the radius of the fillets. The specimens are machined by laser cutting with accuracy of ± 0.1 mm. We distinguish between samples used in the quasi-static tests and samples used in the dynamic tests. The quasi-static specimens, identical to those used in [43], have a gauge length of 20 mm. Note that the quasi-static tests are a requisite to characterize the mechanical response of the material rather than a specific goal of this investigation. The dynamic samples are machined with six different gauge lengths: type 1 with 20 mm, type 2 with 40 mm, type 3 with 60 mm, type 4 with 80 mm, type 5 with 100 mm and type 6 with 140 mm. The dynamic tests are performed in order to uncover the interplay between specimen gauge length, the impact velocity and the fracture location, as further discussed in section 3. Whether it is a quasi-static or dynamic experiment, at least three repeats are conducted.

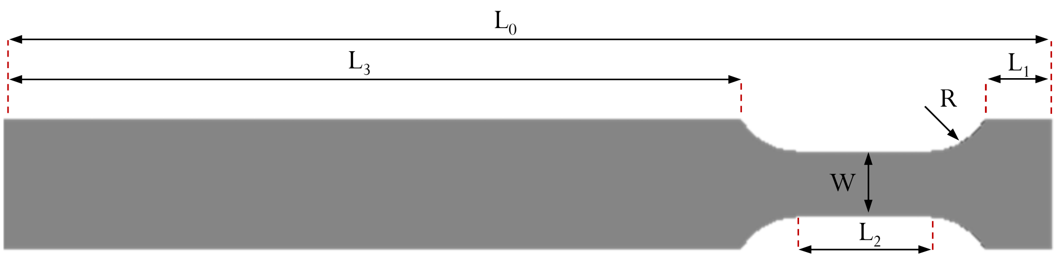

Static specimens

L_0	L_1	L_2 (gauge length)	L_3	W	R
120	41.34	**20**	41.34	10	10

Dynamic specimens

	L_0	L_1	L_2 (gauge length)	L_3	W	R
Type 1	500	41.34	**20**	421.34	10	10
Type 2			**40**	401.34		
Type 3			**60**	381.34		
Type 4			**80**	361.34		
Type 5			**100**	341.34		
Type 6			**140**	301.34		

Figure 1: Geometry and dimensions of the specimens used in the static and dynamic experiments.

2.2. Quasi-static testing

The quasi-static experiments at room temperature were conducted using a servo-hydraulic testing machine INSTRON 8516 100kN under displacement control. We tested specimens whose loading direction formed angles of 0° (parallel), 45° and 90° (perpendicular) with the rolling direction of the plate. The goal was to investigate whether the material displays anisotropy caused by the rolling of the plate. Experiments were conducted for three (initial) strain rates: $\dot{\varepsilon}_0 = 10^{-3}\ s^{-1}$, $\dot{\varepsilon}_0 = 10^{-2}\ s^{-1}$ and $\dot{\varepsilon}_0 = 10^{-1}\ s^{-1}$. In all the experiments the axial strain in the specimen is calculated relying on the cross-head displacement of the machine which has been corrected with knowledge of the elastic modulus of the material as described, for instance, in [44].

Fig. 2 shows stress-strain curves obtained from specimens tested at $10^{-3}\ s^{-1}$, that have been cut following the three different orientations (0°, 45°, 90°) investigated. It is shown that the orientation plays a minor role in the material behaviour since the three curves (practically) overlap. The yield stress and the strain hardening of the material are mild, and the onset of flow localization occurs for ~ 0.2.

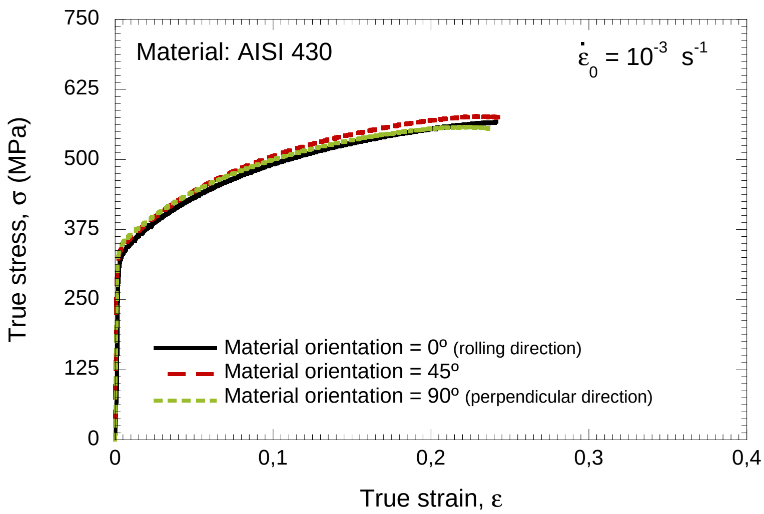

Figure 2: Experimental stress-strain curves for AISI 430 at $T_0 = 300\ K$ and $10^{-3}\ s^{-1}$.

Similarly, we have observed that for $10^{-2}\ s^{-1}$ and $10^{-1}\ s^{-1}$ the orientation barely affects the stress-strain characteristics of the material. Relying on these observations we assume that the in-plane mechanical behaviour can be considered isotropic. From now on, all other experimental results we show are obtained from specimens cut parallel to the rolling direction.

Additionally to quasi-static room temperature tests, we conducted experiments at elevated temperatures $T_0 = 375\ K$, $T_0 = 425\ K$ and $T_0 = 475\ K$. A heating furnace SERVOSIS Split was installed on a servo-hydraulic testing machine INSTRON 8516 100kN. The experiments were conducted under displacement control. For all these tests, the (initial) strain rate was $10^{-2}\ s^{-1}$. Fig. 3 shows that the stress-strain characteristic is slightly shifted downwards as the testing temperature increases, revealing the temperature sensitivity of the material within the range of testing temperatures considered.

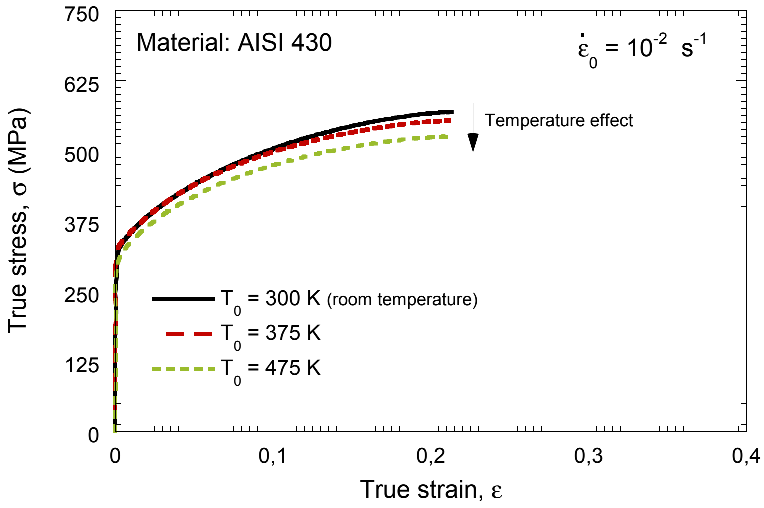

Figure 3: Experimental stress-strain curves for AISI 430 at $10^{-2}\ s^{-1}$ and three different testing temperatures $T_0 = 300\ K$, $T_0 = 375\ K$ and $T_0 = 475\ K$.

2.3. Dynamic testing

Dynamic tensile tests at room temperature are conducted using a high-speed testing machine Instron VHS within the range of impact velocities $1\ m/s \leq V_0 \leq\ 7.5\ m/s$. For the dynamic samples shown in Fig. 1, this set of impact velocities leads to a wide range of (initial) strain rates $7.15\ s^{-1}\ \leq \dot{\varepsilon}_0 \leq\ 375\ s^{-1}$.

The gripping system incorporated in the Instron VHS is the so-called Fast Jaw system. This system relies on two gripping faces being initially held apart by a pair of angled wedges. The actuator initially accelerates downwards with the specimen passing freely between the grips. At the desired location the wedges are knocked out by a set of adjustable rods. This action releases the force of four pretensioned bolts, so causing a set of grips to clamp onto the specimen surface, applying the high velocity loading. This explanation, and further details on the operation mode of the Instron VHS machine, can be found in the work of Battams [45].

Note that the ringing period of the raw data registered from the machine is $\sim 157\ \mu s$. This value corresponds to an eigenfrequency of the piezoelectric load cell of $\sim 6.4\ kHz$, as further verified using the Welch's Power Spectral Density estimation preimplemented in MATLAB. A band-pass Butterworth IIR Filter with a zero-phase forward and reverse procedure (to correct the associated delay of the signal) has been designed in MATLAB to filter the raw stress-strain curves. As further discussed by Rusinek et al. [33], this type of filtering process is usually applied to analyse the stress-strain characteristics obtained from dynamic tensile experiments performed using fast servo-hydraulic machines.

Fig. 4 shows stress-strain curves obtained for different loading rates using specimens with gauge length $L_2 = 20\ mm$. Dynamic (filtered) experimental curves for $\dot{\varepsilon}_0 = 87.5\ s^{-1}$ and $\dot{\varepsilon}_0 = 250\ s^{-1}$ are compared with the stress-strain characteristic obtained for $\dot{\varepsilon}_0 = 10^{-3}\ s^{-1}$. The material shows significant strain rate sensitivity within the range of strain rates tested.

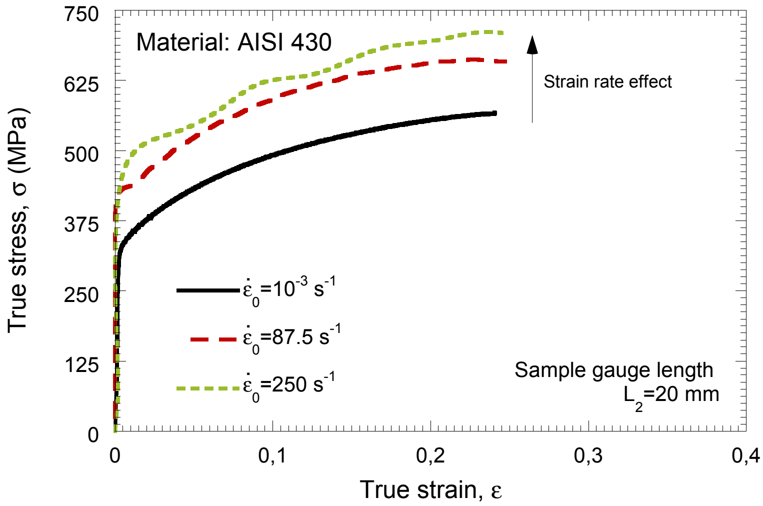

Figure 4: Experimental stress-strain curves for AISI 430 at $T_0 = 300\ K$ and three different initial strain rates: $\dot{\varepsilon}_0 = 10^{-3}\ s^{-1}$, $\dot{\varepsilon}_0 = 87.5\ s^{-1}$ and $\dot{\varepsilon}_0 = 250\ s^{-1}$.

3. Analysis and results: experiments

In this section we show selected dynamic experiments for different gauge lengths and impact velocities. The goal is to show an experimental verification of the deterministic character of the flow localization in the dynamic tensile test. The complete set of dynamic experiments that we have carried out is shown in Appendix A.

Fig. 5 shows three post-mortem samples with gauge length $L_2 = 100\ mm$ tested at $V_0 = 5\ m/s$. It has to be highlighted that, in the three repeats conducted of this test, we have obtained the same failure location. The specimen fails close to the clamped (opposite) side. According to Rodríguez-Martínez et al. [46], the fact that the failure is located away from the middle of the gauge clearly indicates that the specimen is not in (complete) equilibrium during loading. As discussed in the introductory section, the lack of equilibrium in dynamic testing of long tensile samples was reported, for instance, by Lubliner [27] and Botte et al. [28, 29]. Moreover, note that plastic localization develops by the intersection of a pair of necking bands that, in agreement with the theoretical and numerical predictions reported by Storen and Rice [47] and Zhang and Ravi-Chandar [48], are aligned with the directions of zero stretch rate. One of these two bands, the one which develops faster, leads to the final fracture of the specimen. Note that there is (relatively) little reduction of the samples-width within the area surrounding the failure location. The width-reduction of the samples is largely uniform along the gauge.

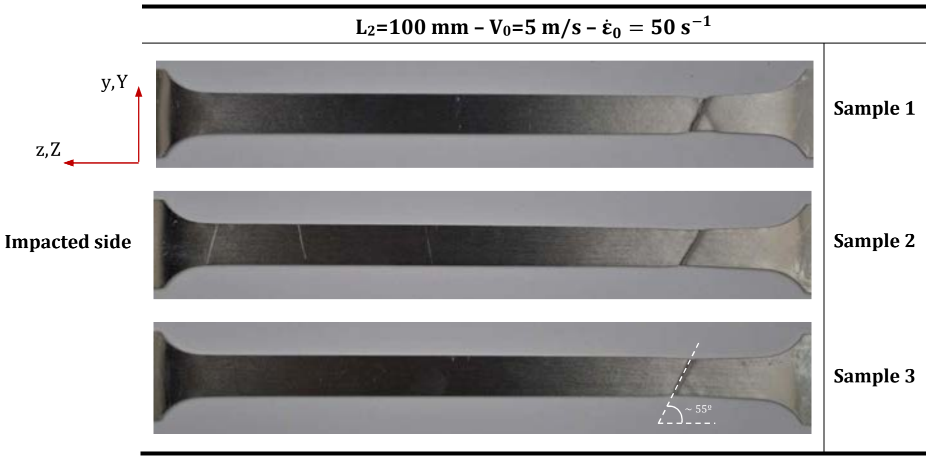

Figure 5: Three post-mortem samples with gauge length $L_2 = 100\ mm$ tested at $V_0 = 5\ m/s$.

The repeatability in the failure location of the dynamic samples is further illustrated in Fig. 6 where we show three post-mortem samples with gauge length $L_2 = 140\ mm$ tested at $V_0 = 1.75\ m/s$. The failure of the sample always occurs close to the middle of the gauge. This does not necessarily imply that the sample is in equilibrium, but it simply exposes that the failure location depends on the applied velocity and the gauge length, as further discussed in sections 3.1 and 3.2. In other words: (1) if the failure locus is located away from the middle of the gauge we know that the sample is not in equilibrium but (2) the fact that the failure locus is located in the middle of the gauge does not ensure that the sample is in equilibrium, see Rodríguez-Martínez et al. [46] for details. Moreover, it has to be noted that, in comparison with the results shown in Fig. 5, now there is larger width-reduction of the gauge in the vicinity of the fracture point. The pair of localization bands are located inside a necked region in the $\{Y, Z\}$ plane. The width-reduction is not uniform along the gauge. The aspect ratio of the specimen gauge seems to play a strong role in the failure location and in the failure pattern, as further discussed in forthcoming sections of this paper.

To be noted that, as detailed in Appendix A, we have obtained very high repeatability in the failure location for all the gauge lengths explored and within the whole range of impact velocities tested. This indicates that, rather than being random, the position where the flow localization

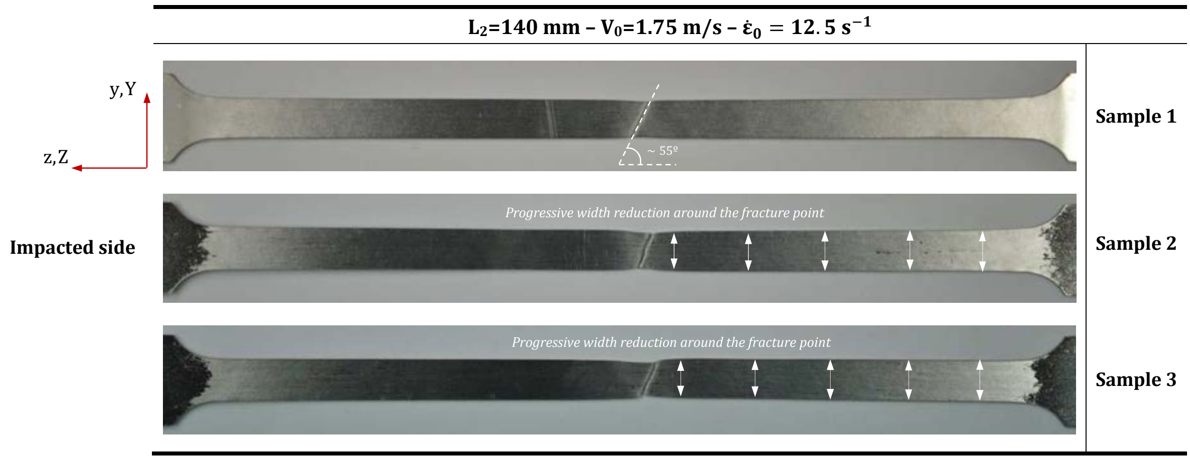

Figure 6: Three post-mortem samples with gauge length $L_2 = 140\ mm$ tested at $V_0 = 1.75\ m/s$.

occurs is deterministic. Exceptions occurred in few cases for which one of the three repeats programmed showed different failure location than the other two. In these selected cases we decided to perform an additional test after which we always had three (of four) samples with the same failure location. This failure location was assumed to be the representative of such sample geometry and loading conditions. The fact that one of the tests is not providing the same fracture location than the other three is simply attributed to the inherent uncertainties surrounding experimentation. Our belief is that slight variations in (1) the pressure applied by the jaws to fix the samples during testing and/or (2) the actual velocity applied by the machine are responsible for the small scatter that we have registered in the fracture location.

3.1. Influence of loading velocity on the location of flow localization

In this section we analyse the influence of loading velocity on the fracture location. Fig. 7 shows seven samples with gauge length $L_2 = 60\ mm$ tested at different velocities. For the smallest impact velocity that we have explored $V_0 = 1\ m/s$ the failure location occurs close to the impacted side. Increasing the impact velocity changes the place where the failure occurs. Thus, for $V_0 = 1.75\ m/s$, $V_0 = 2.5\ m/s$, $V_0 = 3.75\ m/s$, $V_0 = 5\ m/s$ and $V_0 = 6.25\ m/s$, we observe that the sample breaks near the clamped side. Finally, for the highest velocity tested $V_0 = 7.5\ m/s$ the fracture location moves again to the impacted side. Note that such a strong interplay between impact velocity and failure location has been found for the largest sample gauge lengths investigated. These experimental results bear a definite resemblance to those recently reported by Osovski et al. [39], Rittel et al. [40] and Rotbaum et al. [49] using cylindrical samples, and confirm the numerical predictions reported by Rusinek et al. [36] and Rodríguez-Martínez et al. [50] using flat samples who claimed that the failure location in the dynamic tensile test is very much controlled by the impact velocity. Since the sample is initially at rest, the fact that the fracture location is controlled by the impact velocity means that the dynamic effects (stress waves and inertia) dictate the fracture location. We will further deepen into these experimental findings using the finite element calculations in section 6.1.

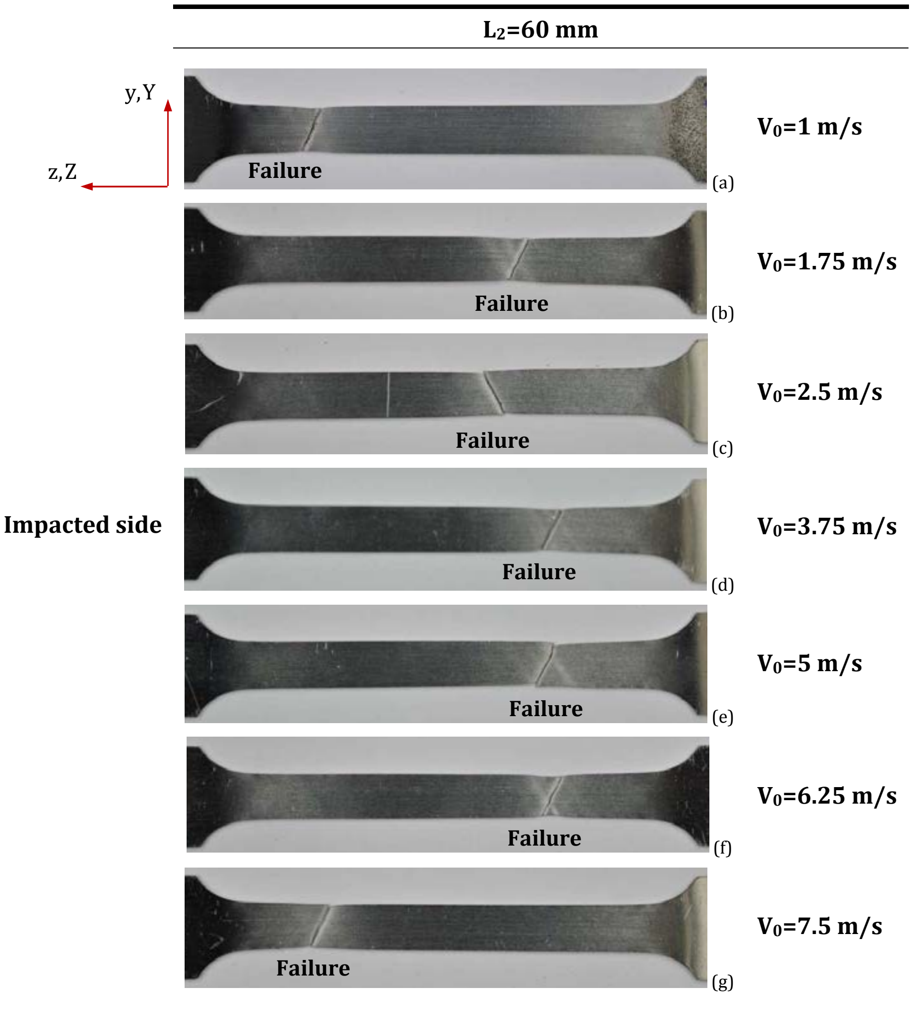

Figure 7: Seven post-mortem samples with gauge length $L_2 = 60\ mm$ tested at: (a) $V_0 = 1\ m/s$, (b) $V_0 = 1.75\ m/s$, (c) $V_0 = 2.5\ m/s$, (d) $V_0 = 3.75\ m/s$, (e) $V_0 = 5\ m/s$, (f) $V_0 = 6.25\ m/s$, (g) $V_0 = 7.5\ m/s$.

3.2. Influence of specimen gauge length on the location of flow localization

Relying on the experimental results shown above, we expect that the gauge length will play a role in the fracture location. For different gauge lengths the stress waves need different times to go over the entire gauge, which alters the processes of reflection and interaction of waves taking place in the sample during the test. Further, we expect that the gauge length will affect the fracture pattern. Note that the gauge length determines the aspect ratio (slenderness) of the gauge which, on the basis of the results shown in Figs. 5 and 6, plays a role in the failure mode.

Fig. 8 shows six specimens with different gauge lengths tested at $V_0 = 5\ m/s$. In the case of $L_2 = 20\ mm$ the failure occurs in the middle of the gauge with negligible (localized) width-reduction near the fracture location. To be noted that, instead of having a single localization point which leads to fracture as in the specimens shown in Figs. 5, 6 and 7, there are traces of multiple localization bands all along the gauge. This key (and very uncommon) finding will be discussed in detail in the next section. By now, we just focus on the role played by gauge length in the fracture location. It is observed that for $L_2 = 40\ mm$ the failure is no longer in the middle of the gauge but close to the impacted side, whereas for $L_2 = 60\ mm$, $L_2 = 80\ mm$ and $L_2 = 100\ mm$ the fracture is located near the clamped side. Surrounding the failure point, the thinning of the sample along the Y direction increases with the gauge length. Finally, for the greatest gauge length $L_2 = 140\ mm$ the fracture location is located in the middle of the gauge. There is a significant reduction of the width of the gauge around the fracture point. The sample straining is not uniform along the gauge.

A close relation between gauge length, failure location and failure pattern has been found for all the impact velocities tested, which confirms the control that dynamic effects (stress waves and inertia) have over the failure location and the failure mode of the sample. Further, we claim that the extensive experimental campaign that we have conducted in this investigation strengthens the idea that the failure location in the dynamic tensile test is deterministic. Instead of being controlled by random-type effects as intrinsic material defects, the failure location is governed to a large extent by dynamic phenomena.

3.3. Multiple localization pattern

Multiple, and largely regular, localization patterns have been observed in a significant number of the experiments performed using the samples with the shorter gauge lengths. Four of these samples are shown in Fig. 9. For $L_2 = 20\ mm$ we have found multiple necking bands in $\sim 45\%$ of the samples tested at velocities larger than $V_0 = 3.75\ m/s$. For $L_2 = 40\ mm$ the multiple localization pattern is observed in $\sim 35\%$ of the experiments. For $L_2 = 60\ mm$ we only have observed multiple necking bands in two samples tested at $V_0 = 1.75\ m/s$ and $V_0 = 5\ m/s$. For all the samples with $L_2 = 80\ mm$, $L_2 = 100\ mm$ and $L_2 = 140\ mm$ only a pair of necking bands are formed, these being

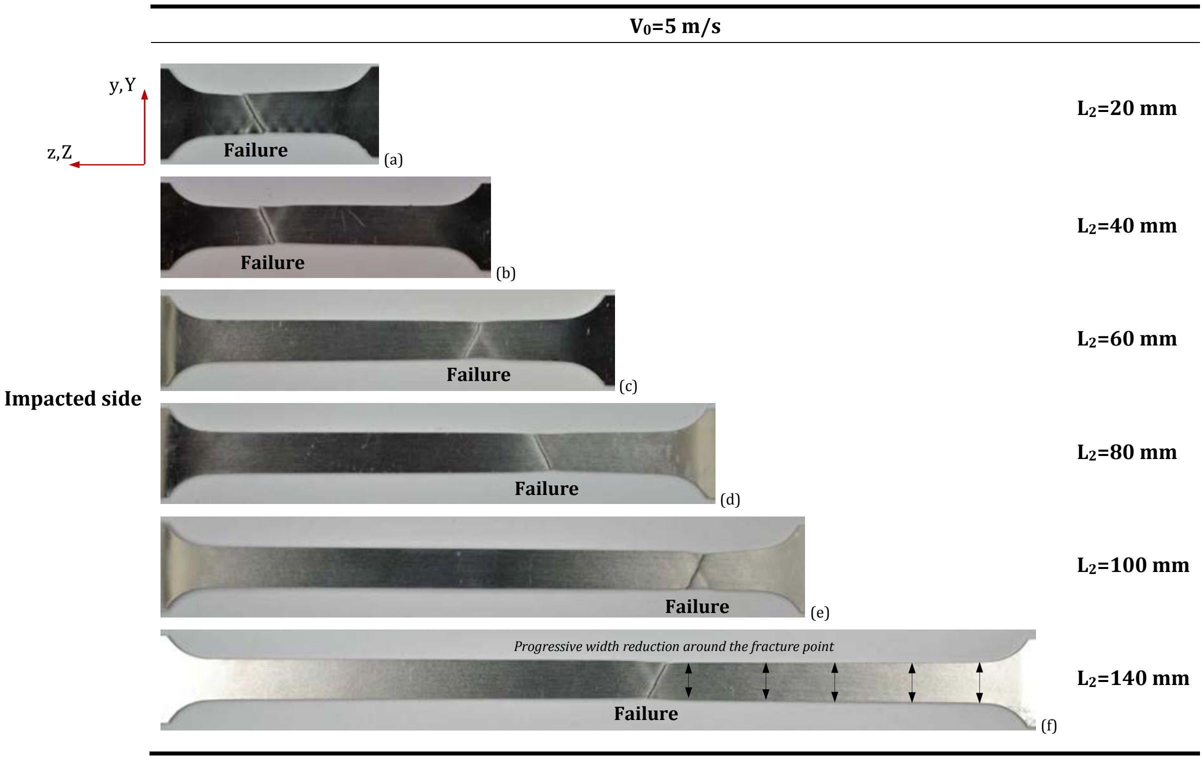

Figure 8: Six post-mortem samples with different gauge lengths tested at $V_0 = 5\ m/s$: (a) $L_2 = 20\ mm$, (b) $L_2 = 40\ mm$, (c) $L_2 = 60\ mm$, (d) $L_2 = 80\ mm$, (e) $L_2 = 100\ mm$, (f) $L_2 = 140\ mm$.

responsible for the specimen fracture. It follows from previous results that short samples tested at high impact velocities are more prone to develop multiple localization bands. This behaviour may be explained based on the following premises: (1) the shortest samples (shortest aspect ratios L_2/W in Fig. 1) are the most equilibrated during testing [22, 29], develop the most uniform strain distribution along the gauge and do not show (localized) width-reduction near the fracture point; (2) increasing impact velocity boosts the role played by inertia in the material response [51, 52]. These two ideas are developed below:

1. A tensile sample with constant cross section tested under *perfect* mechanical equilibrium shall develop uniform strain distribution along the gauge (i.e. constant width-reduction along the gauge) leading to regular and symmetric localization and failure patterns (in the absence of significant material defects). In the absence of *perfect* equilibrium, the specimen is susceptible to show variability in the strain field along the gauge (i.e. variable width-reduction along the gauge) leading to irregular and unsymmetrical localization and failure patterns. On these basis, it is reasonable to assume that a specimen tested under conditions close to equilibrium is more likely to develop regular and symmetric localization and failure patterns than a

sample tested under loading conditions which are far from mechanical equilibrium, as further discussed in section 6.3.

On the one hand, these arguments explain that almost all the specimens that we have tested under (quasi)static loading, and therefore under loading conditions very close to mechanical equilibrium, failed in the middle of the sample, i.e. they have shown a symmetric failure pattern. On the other hand, these arguments also explain that most of the shortest samples (shortest aspect ratio L_2/W) tested under dynamic loading show symmetric localization and failure patterns. Note that in these samples (1) the localization pattern is repetitive and largely symmetric with the respect to the longitudinal and transversal axes of the specimens and (2) the samples fail in (approximately) the middle of the gauge.

2. An equilibrated tensile specimen tested under dynamic loading is prone to develop multiple localization points. This behaviour is frequently observed in the radial expansion of axially symmetric structures like rings [53, 54], tubes [55, 56] and hemispheres [57]. The symmetry of these structures nearly eliminates the effects of wave propagation before the onset of plastic localization, the specimen being tested under loading conditions close to equilibrium. All these experimental works reported that the number of localization points increases with the loading velocity. This experimental finding has been explained by several authors [58, 59] who claimed that inertia, via strain rate, is the main responsible for the development of multiple localization patterns in samples tested under dynamic loading. These arguments explain that we have observed multiple necking bands mostly in those samples that we have tested at the higher strain rates.

4. Constitutive model

The main hypothesis of the constitutive model used to describe the thermoviscoplastic behaviour of the AISI 430 steel centers on the standard principles of Huber-Mises plasticity: additive decomposition of the rate of deformation tensor, isotropic hardening, associated flow rule and plastic power equivalence

$$\boldsymbol{\sigma}^{\nabla} = \mathbf{C} : \mathbf{d}^{e} = \mathbf{C} : \left(\mathbf{d} - \mathbf{d}^{p} - \mathbf{d}^{\theta}\right) \tag{1}$$

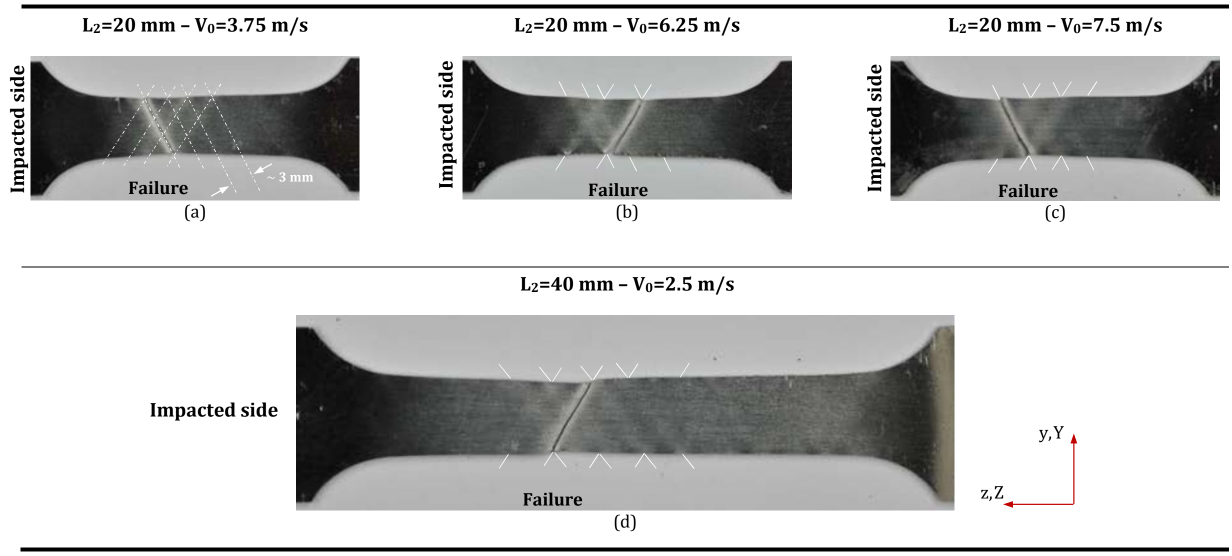

Figure 9: Four post-mortem samples with different gauge lengths tested at different velocities. Multiple localization bands are observed in all of them. (a) $L_2 = 20\ mm$ and $V_0 = 3.75\ m/s$, (b) $L_2 = 20\ mm$ and $V_0 = 6.25\ m/s$, (c) $L_2 = 20\ mm$ and $V_0 = 7.5\ m/s$ and (d) $L_2 = 40\ mm$ $V_0 = 2.5\ m/s$.

$$\Psi = \bar{\sigma} - \sigma_Y = 0 \tag{2}$$

$$\mathbf{d}^p = \frac{\partial \Psi}{\partial \boldsymbol{\sigma}} \dot{\bar{\varepsilon}}^p = \frac{3\mathbf{s}}{2\bar{\sigma}} \dot{\bar{\varepsilon}}^p \tag{3}$$

where $\boldsymbol{\sigma}^{\nabla}$ is an objective derivative of the Cauchy stress tensor, $\mathbf{d}$, $\mathbf{d}^e$, $\mathbf{d}^p$ and $\mathbf{d}^\theta$ are the total, elastic, plastic and thermal rate of deformation tensors respectively, $\mathbf{C}$ is the Hooke tensor for isotropic elasticity (defined by Young modulus E and Poisson ratio ν), Ψ the yield function, $\bar{\sigma}$ the equivalent stress, σ_Y is the yield stress, $\mathbf{s}$ the deviatoric stress tensor and $\dot{\bar{\varepsilon}}^p$ is the equivalent plastic strain rate.

The yield stress is given as a function of the equivalent plastic strain $\bar{\varepsilon}^p$, the equivalent plastic strain rate $\dot{\bar{\varepsilon}}^p$ and the temperature T through the following power-type relation

$$\sigma_Y = A + B \left(\bar{\varepsilon}^p\right)^n \left(\frac{\dot{\bar{\varepsilon}}^p}{\dot{\bar{\varepsilon}}_{ref}}\right)^m \left(\frac{T}{T_{ref}}\right)^{-\mu} \tag{4}$$

The identification of the yield stress parameters is conducted by a numerical regression based on experimental data obtained (only) with the samples of gauge length 20 mm at different strain rates and temperatures. Relying on finite element calculations, we have checked that these specimens reach equilibrium during the experiments. This result agrees with previous observations reported by Rusinek et al. [36] and Klepaczko [60]. Conventional material constants, elastic parameters and parameters related to the yield stress for AISI 430 steel are given in Table 2.

Symbol	Property and units	Value
ρ_o	Initial density (kg/m^3)	7740
C_p	Specific heat (J/kgK), Eq. (5)	460
k	Thermal conductivity (W/mK), Eq. (5)	26.1
α	Thermal expansion coefficient (K^{-1}), Eq. (5)	0.00001
E	Young modulus (GPa)	200
ν	Poisson ratio	0.33
A	Initial yield stress (MPa), Eq. (4)	175.67
B	Work hardening modulus (MPa), Eq. (4)	530.13
n	Work hardening exponent, Eq. (4)	0.167
$\dot{\varepsilon}_{ref}$	Reference strain rate (s^{-1}), Eq. (4)	0.01
m	Strain rate sensitivity exponent, Eq. (4)	0.0118
T_{ref}	Reference temperature (K), Eq. (4)	300
μ	Temperature sensitivity exponent, Eq. (4)	0.51
β	Taylor-Quinney coefficient, Eq. (5)	0.9

Table 2: *Conventional material constants, elastic parameters and parameters related to the yield stress for AISI 430 steel.*

No doubt, more sophisticated constitutive descriptions could be used to model the material behaviour (see e.g. [61, 62]). Nevertheless we claim that the simple modelling presented here is sufficient to develop reliable numerical computations to uncover the key issues which control the deterministic character of plastic flow localization in the dynamic tensile test.

5. Finite element model

This section describes the features of the 3D finite element models developed to simulate plastic strain localization in AISI 430 steel sheets subjected to dynamic tension. The numerical analyses are carried out using the finite element code ABAQUS/Explicit [41]. To be noted that the goal of the numerical calculations is not to mimic the experimental tests but to provide new insights into the role played by dynamic effects (inertia and wave disturbances) and boundary conditions in the deterministic character of the plastic flow localization. For that purpose is enough to use simple geometrical models which solely consider the gauge of the sample, as further demonstrated in section 6. This greatly simplifies the interpretation of the finite element results and reduces the computational cost. Thus, our problem setting is a strip with thickness $h = 1\ mm$, width $W = 10\ mm$ (unless otherwise stated, see section 6.3) and six different lengths L_2, according to the six gauge lengths used in the dynamic samples described in Fig. 1. On these geometrical basis, two different types of finite element models are developed. The idea is that the comparison between the results obtained with these two models which are described below will allow to explore the respective influence of dynamic effects and boundary conditions on flow localization. Note that $\{x, y, z\}$ denotes the Eulerian coordinate system while $\{X, Y, Z\}$ refers to the Lagrangian.

- **Model A: No-field configuration**. The solid is initially at rest. The loading conditions are $V_Z(X, Y, L_2, t) = V_0 = \dot{\varepsilon}_0 L_2$ and $V_Z(X, Y, 0, t) = 0$ (see the Lagrangian coordinate system defined in the figure). Application of these loading conditions leads to the propagation of stress waves along the sample [63, 64], precluding –full/complete– mechanical equilibrium. Within model A we distinguish 2 configurations:

  - **Model A-1**. No additional constraints are imposed to the displacements of the nodes of the model. This configuration is representative of a typical experimental test.
  - **Model A-2**. The nodes of the workpiece located at the surfaces $\{X, \pm\frac{W}{2}, Z\}$ have identical displacement along the Y axis during the calculation. Using Hencky strain as our strain measure, and relying on the incompressibility of the plastic flow, we set $u_Y(X, \pm W/2, Z, t) = \mp\frac{W}{2}\left(\frac{1}{\sqrt{\dot{\varepsilon}_0 t + 1}} - 1\right)$. This configuration tries to emulate an infinitely long sample along the Y axis.

  Note that, due to the symmetry of the model, only the $\{X > 0, Y > 0\}$ quarter of the specimen has been analysed (see Fig. 10).

- **Model B: Field configuration**. The initial condition corresponds to an equilibrium configuration which *virtually* prevents the generation of stress waves during the loading process. We say *virtually* because, due to the discretization of the workpiece and the explicit integration scheme used by the FE code, slight disturbances in the field variables are generated during the simulations. These little perturbations are required to trigger plastic flow localization as shown by Rusinek and Zaera [65]. Nevertheless, we claim that in comparison with the *no-field* condition, now the role played by the stress waves in the sample's response is significantly reduced [46, 59]. The loading conditions are $V_Z(X, Y, \pm\frac{L_2}{2}, t) = \pm\frac{V_0}{2} = \pm\dot{\varepsilon}_0\frac{L_2}{2}$ (see the Lagrangian coordinate system defined in the figure). The initial equilibrium state is obtained by initializing the velocity, stress, strain and displacement fields in the sample. The initial conditions in velocity, formulated based on Zaera et al. [59], are $V_X(X, Y, Z, 0) = -\nu\dot{\varepsilon}_0 X$, $V_Y(X, Y, Z, 0) = -\nu\dot{\varepsilon}_0 Y$ and $V_Z(X, Y, Z, 0) = \dot{\varepsilon}_0 Z$. The initial conditions in stress are $\sigma_X(X, Y, Z, 0) = 0$, $\sigma_Y(X, Y, Z, 0) = 0$ and $\sigma_Z(X, Y, Z, 0) = \rho_0 C\dot{\varepsilon}_0\frac{L_2}{2}$, where $C = \sqrt{E/\rho_0}$ is the longitudinal elastic wave speed. Note that this procedure for initializing the stress field has to be limited to the cases for which $\rho_0 C\dot{\varepsilon}_0\frac{L_2}{2} < A$, where it has to be recalled that A in Eq. (4) defines the initial yield stress of the material. Previous expression implies that the maximum loading velocity V_0 that can be investigated using this procedure is 8.92 m/s. With the knowledge of the initial stress field, and relying on the Hooke's law, we calculate the initial strains as $\epsilon_X(X, Y, Z, 0) = -\frac{\nu\rho_0 C\dot{\varepsilon}_0 L_2}{2E}$, $\epsilon_Y(X, Y, Z, 0) = -\frac{\nu\rho_0 C\dot{\varepsilon}_0 L_2}{2E}$ and $\epsilon_Z(X, Y, Z, 0) = \frac{\rho_0 C\dot{\varepsilon}_0 L_2}{2E}$. Using Hencky strain we calculate the initial displacements as $u_X(X, Y, Z, 0) = -\frac{X}{2}\left(\exp^{-\frac{\nu\rho_0 C\dot{\varepsilon}_0 L_2}{2E}} - 1\right)$, $u_Y(X, Y, Z, 0) = -\frac{Y}{2}\left(\exp^{-\frac{\nu\rho_0 C\dot{\varepsilon}_0 L_2}{2E}} - 1\right)$ and $u_Z(X, Y, Z, 0) = Z\left(\exp^{\frac{\rho_0 C\dot{\varepsilon}_0 L_2}{2E}} - 1\right)$. It is worth mentioning that this *initialization methodology* is an original contribution of this paper since it significantly improves the procedure proposed by Rodríguez-Martínez et al. [46], where only the velocity along the loading direction was initialized in the so-called field configuration. As for model A, we also distinguish 2 configurations for model B:

– **Model B-1**. No additional constraints are imposed to the displacements of the nodes of the model.

– **Model B-2**. The displacement of the nodes located at the surfaces $\{X, \pm W/2, Z\}$ is prescribed as $u_Y(X, \pm W/2, Z, t) = \mp\frac{W}{2}\left(\exp^{-\frac{\nu\rho_0 C\dot{\varepsilon}_0 L_2}{2E}} + \frac{1}{\sqrt{\dot{\varepsilon}_0 t + 1}} - 2\right)$. The first term inside the parenthesis refers to the displacement due to the initialization of the field variables while the send term corresponds to the time dependent displacement calculated based on the incompressibility of the plastic flow, as previously described for model A-2.

Note that, due to the symmetry of the model, only the $\{X > 0, Y > 0, Z > 0\}$ eight of the specimen has been analysed (see Fig. 10).

Models A-2 and B-2 will serve to explain the role played by boundary conditions in the post-uniform elongation of the sample and, specifically, in the failure pattern. Further, the fact that the boundary condition $u_Y(X, \pm W/2, Z, t)$ imposed to the models A-2 and B-2 emulates an infinitely long sample in the Y axis will serve to highlight the influence of the sample slenderness on the formation of multiple localization patterns.

Moreover, we have considered a *fully coupled* thermo-mechanical framework in which, assuming no heat flow at the workpiece boundaries, the relationship between the spatial-temporal variation of the temperature T and the dissipative and thermoelastic heat generation rates is as follows

$$k\nabla^2 T - \rho C_p \dot{T} = -\beta \boldsymbol{\sigma} : \mathbf{d}^p + \alpha \left(3\lambda + 2\mu\right) T_0 \mathbf{d}^e : \mathbf{1} \tag{5}$$

where k is the thermal conductivity, ρ is the current material density, C_p is the specific heat, β is the Taylor-Quinney coefficient and α is the thermal expansion coefficient. Moreover λ and μ are the Lamé constants, and T_0 is the initial temperature that has been set to 300 K in all cases. Note that $\mathbf{d}^e : \mathbf{1}$ is the trace of the elastic rate of deformation tensor.

The finite element models are meshed using eight node coupled displacement-temperature solid elements, with reduced integration and hourglass control ($C3D8RT$). The elements have an initial aspect ratio $1:2:1$ with dimensions $0.166 \times 0.333 \times 0.166$ mm^3 for all the models that we have built. We have checked that, with the increase of plastic deformation in the workpiece, the shape of the elements evolves, approaching an aspect ratio closer to $1:1:1$ at the time of flow localization. According to Zukas and Scheffer [66], such an element shape is optimal for describing dynamic events like high rate flow localization. Further, a mesh convergence study has been performed, and the time evolution of different critical output variables, namely stress, strain and necking inception, were compared against a measure of mesh density until the results converged satisfactorily (see Appendix B for details). Note that, in our modelling, viscosity, inertia and thermal conductivity act as potent regularization factors that help to the well-possessedness of the problem at hand

[67, 68]. We hold that this minimizes the spurious influence of the mesh in the solution of the boundary value problem.

The set of constitutive equations describing the material behaviour presented in section 4 are implemented in the finite element code through a user subroutine following the procedure developed by Zaera and Fernández-Sáez [69]. For integration of the set of constitutive equations in a finite deformation framework, incremental objectivity is achieved by rewriting them in a corotational configuration [70, 71], defined in ABAQUS/Explicit by the polar rotation tensor. The stress is updated with the radial return algorithm

$$\boldsymbol{\sigma}_{n+1} = \boldsymbol{\sigma}_{n+1}^{trial} - 3G\Delta\bar{\varepsilon}^p \frac{\mathbf{s}_{n+1}}{\bar{\sigma}_{n+1}} \tag{6}$$

where G is the elastic shear modulus and $\boldsymbol{\sigma}_{n+1}^{trial}$ is the trial stress is defined by

$$\boldsymbol{\sigma}_{n+1}^{trial} = \boldsymbol{\sigma}_n + \mathbf{C} : \Delta\boldsymbol{\varepsilon} \tag{7}$$

According to the properties of radial return, the equivalent stress may be updated with the following equation

$$\bar{\sigma}_{n+1} = \bar{\sigma}_{n+1}^{trial} - 3G\Delta\bar{\varepsilon}^p \tag{8}$$

and the yield condition Eq. (2) which, coupled to Eq. (4), permits to obtain the equivalent plastic strain increment $\Delta\bar{\varepsilon}^p$.

6. Analysis and results: finite element simulations

Next, the experimental findings reported in section 3 are further explained relying on the results obtained from the finite element simulations.

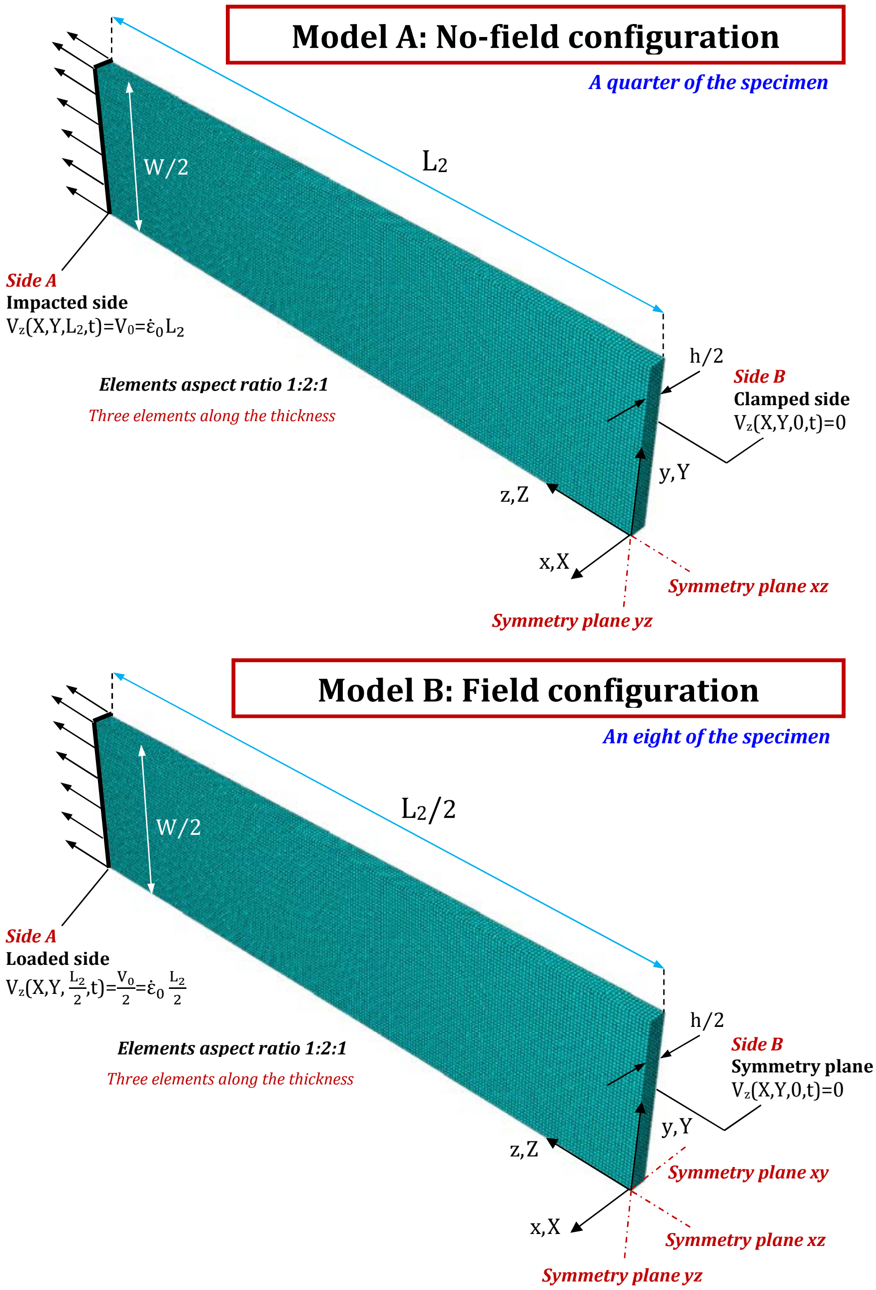

Finite element models

L_2 (mm)					
Type 1	**Type 2**	**Type 3**	**Type 4**	**Type 5**	**Type 6**
20	40	60	80	100	140

Figure 10: 3D finite element models. Mesh, dimensions, boundary conditions and loading conditions of models A and B.

6.1. Influence of loading velocity on the location of flow localization

In order to obtain further insights into the interplay between the impact velocity and the location of flow localization, we rely on finite element simulations conducted using the model A-1. As described in section 5, within the models built in this paper, the A-1 is the most similar to a typical experimental arrangement in terms of initial, loading and boundary conditions. Fig. 11 shows contours of equivalent plastic strain $\bar{\varepsilon}^p$ in the Lagrangian configuration (undeformed shape) for $L_2 = 60\ mm$ and various loading velocities. The range of loading velocities analysed in the calculations is wider than the range covered by the experiments in order to reveal, to the full extent, how the point of localization varies sequentially from side to side of the sample with the increase of the loading velocity. Note that, irrespective of the impact velocity, the plastic strain localization takes the form of a pair of necking bands that follow the directions of zero stretch rate, as shown in the experimental results reported in section 3.

In the case of $V_0 = 0.125\ m/s$, the smallest velocity explored, the localization of plastic deformation is located at the clamped end. The increase in applied velocity moves the localization point towards the impacted side, where it remains until reaching $V_0 = 7.5\ m/s$. Then, plastic localization occurs near the clamped end. For $V_0 = 10\ m/s$ the localization point is back to the impacted side while for $V_0 = 15\ m/s$ it takes place, again, near the clamped end. Such a systematic motion of the localization point along the sample continues taking place if we keep increasing the applied speed, until the critical impact velocity (CIV) is attained for $V_0 \approx 80\ m/s$. When the CIV is reached the applied velocity is such that it generates a plastic wave which induces *(instantaneous)* flow localization [63]. Thus, for velocities above the CIV the localization of plastic deformation inevitably occurs *(instantaneously)* at the impacted side, as shown by Klepaczko [72] and Rusinek et al. [36]. Note that such a strong influence of the impact velocity on the location of flow localization has been found for all the gauge lengths investigated, the so-called types 1-6 in Fig. 10.

It is important to realize that the specific locations of flow localization predicted by the numerical calculations do not agree with their experimental counterparts shown in Fig. 7. While we highlight the qualitative agreement between numerical calculations and experiments, we acknowledge the lack of quantitative agreement. Besides the simplified geometry that we have analysed, we think that there are some other factors, that can hardly be overcome, responsible for this disagreement (quantitative, but not qualitative, disagreement). For instance, there are *uncertainties* intrinsic to the experimental setup related to the loading condition (the actual applied velocity is surely not a *perfect* step-function) and the boundary conditions (the system used to attach the sample does not ensures a *perfect* embedding). We hold that these *uncertainties* make virtually impossible to build a finite element model to mimic the experiments with the accuracy required to predict the specific location of flow localization. Moreover, while in the experiments the stress waves may be transmitted to the machine through the jaws, we do not consider this scenario in our modelling. Nevertheless, we hold that our (simple) calculations are in qualitative agreement with the experiments and show the interplay between the fracture location and the loading velocity. Further, these calculations provide an additional proof of the deterministic character of location of plastic strain localization in the dynamic tensile test.

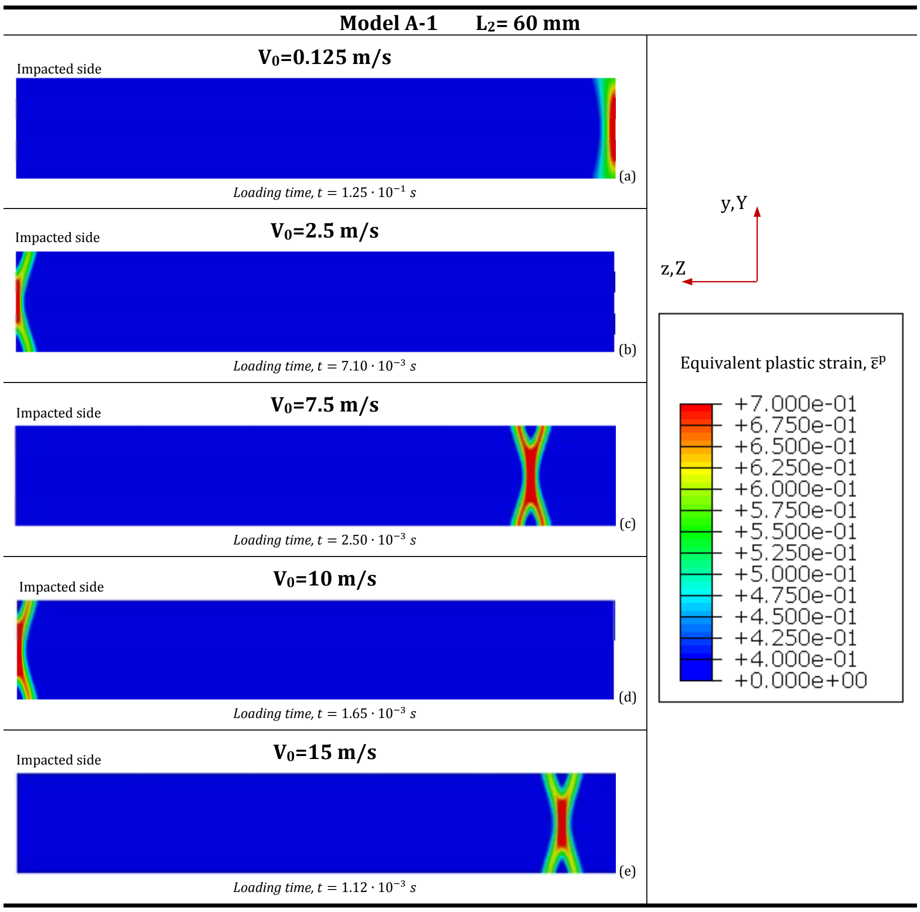

Figure 11: Finite element results. Model A-1. Contours of equivalent plastic strain $\bar{\varepsilon}^p$ in the Lagrangian configuration (undeformed shape) for $L_2 = 60\ mm$ and various impact velocities. (a) $V_0 = 0.125\ m/s$, (b) $V_0 = 2.5\ m/s$, (c) $V_0 = 7.5\ m/s$, (d) $V_0 = 10\ m/s$ and (e) $V_0 = 15\ m/s$.

6.2. Influence of specimen gauge length on the location of flow localization

This section aims at further deepen into the relationship between the sample gauge length and the location of flow localization that was revealed in section 3.2. For that purpose we rely on finite element simulations conducted using the model A-1. Fig. 12 illustrates contours of equivalent plastic strain $\bar{\varepsilon}^p$ in the Lagrangian configuration (undeformed shape) for $V_0 = 5\ m/s$ and various gauge lengths. Note that, irrespective of the sample length, the plastic strain localization takes the form of a pair of necking bands.

In the case of $L_2 = 20\ mm$, the shortest gauge length explored, the localization of plastic deformation is located roughly at the center of the sample. The increase of the gauge length affects the location of flow localization which occurs at the impacted end for $L_2 = 40\ mm$, $L_2 = 60\ mm$ and $L_2 = 80\ mm$. For $L_2 = 100\ mm$ two localization points are detected. The main one (the most developed) takes place at the impacted end, while the secondary one appears at the clamped site. For $L_2 = 140\ mm$ a single localization point appears at the clamped site. Such a systematic motion of the localization point along the sample continues taking place if we keep increasing the sample gauge length. Note that such a strong influence of the gauge length on the location of flow localization has been found for all the applied velocities investigated within the range $0.125\ m/s \lesssim V_0 \lesssim 80\ m/s$ (below the CIV).

Moreover, it has to be highlighted that the case $L_2 = 100\ mm$ shown in Fig. 12 is a transient state, halfway between the localization patterns of $L_2 = 80\ mm$ and $L_2 = 140\ mm$. As such, it reveals the nature of the role played by the sample length in the location of flow localization. We recall here that the gauge length determines the time required by the elastic strains to travel over the whole gauge and, as such, it controls the processes of reflection and interaction of stress waves which dictates the locations where the build up of plastic deformation occurs. These results shall be understood as an additional proof of the deterministic character of the flow localization in the dynamic tensile test.

It is a fact that, because of a number of reasons already discussed in previous section, our calculations do not predict the specific location of flow localization observed in the experiments (qualitative agreement, quantitative disagreement), see Fig. 8. Nevertheless, we hold that they help to provide a proper interpretation of our experimental findings and contribute to reveal the key mechanisms which reside behind the interplay between the gauge length and the fracture location.

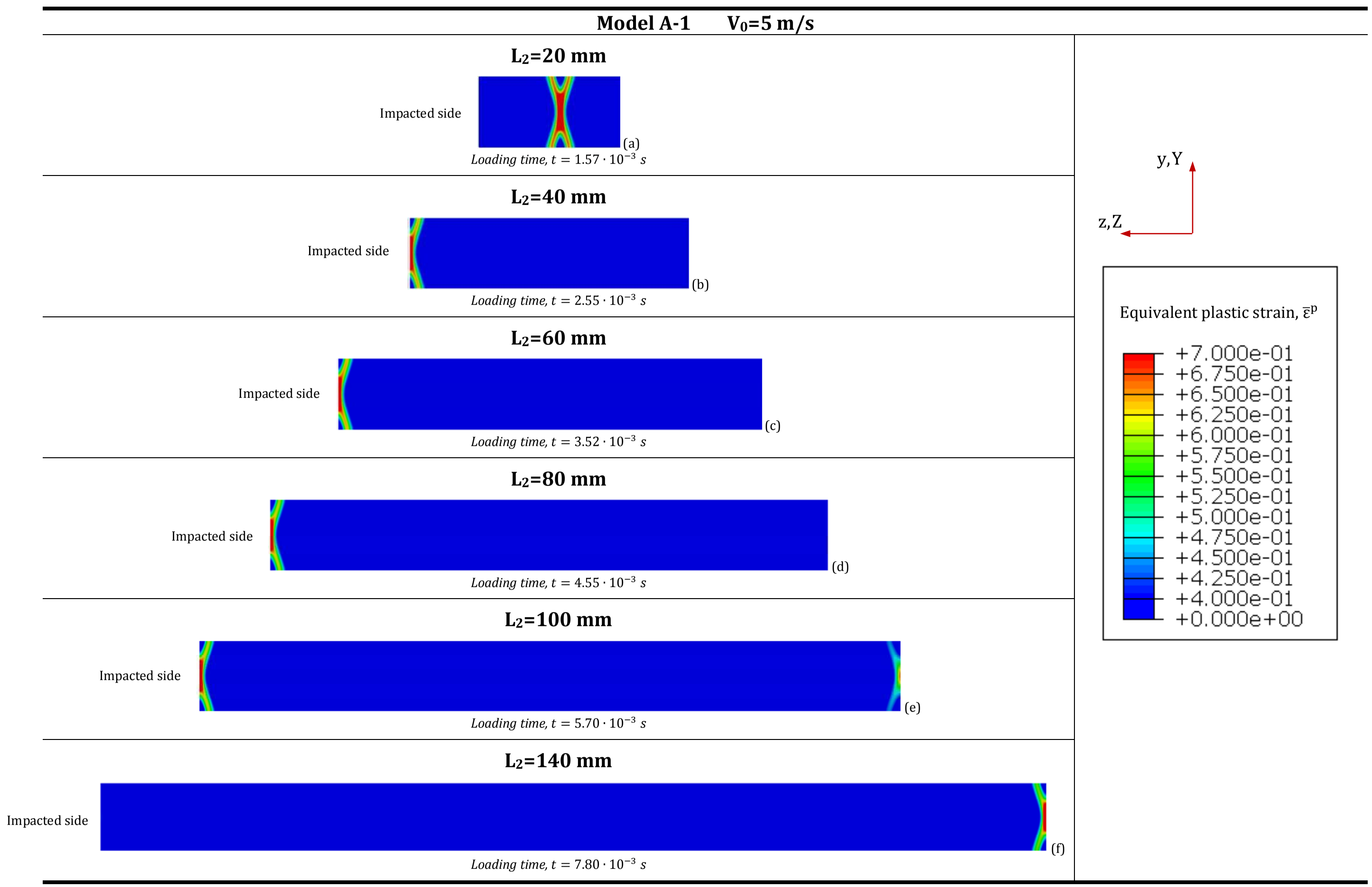

Figure 12: Finite element results. Model A-1. Contours of equivalent plastic strain $\bar{\varepsilon}^p$ in the Lagrangian configuration (undeformed shape) for $V_0 = 5m/s$ and various gauge lengths. (a) $L_2 = 20\ mm$, (b) $L_2 = 40\ mm$, (c) $L_2 = 60\ mm$, (d) $L_2 = 80\ mm$, (e) $L_2 = 100\ mm$ and (f) $L_2 = 140\ mm$.

6.3. Multiple localization pattern

In this section we aim at uncovering the role played by the initial conditions, the boundary conditions and the sample slenderness on the formation of multiple localization patterns. The way in which these factors either favour or preclude the emergence of multiple necking bands has been hardly investigated in the literature [73], thus we intend to give some indications about it here.

Fig. 13 shows contours of equivalent strain rate in Eulerian (deformed shape) configuration for $V_0 = 5\ m/s$ and $L_2 = 20\ mm$. The results for model A-1 are depicted in Fig. 13(a) while the results of model B-1 are illustrated in Fig. 13(b). We have determined the localization strain $\bar{\varepsilon}^p_l$ in the calculations following the procedure reported elsewhere [63, 74]. The localization strain is assumed as given by the condition $\dfrac{d\bar{\varepsilon}^p}{dt} = 0$, where $\bar{\varepsilon}^p$ is measured within the unloading zone which surrounds the localized region. The localization strain obtained for model A-1 is $\bar{\varepsilon}^p_l \approx 0.25$ while for model B-1 is $\bar{\varepsilon}^p_l \approx 0.34$. The retardation of flow localization registered for model B-1 is caused by the initialization of the field variables (see section 5) which minimizes the stress propagation phenomena, boosting mechanical equilibrium and delaying plastic localization [59]. This observation agrees with the theoretical and numerical results presented by different authors [75, 73] who showed that the stress waves disturbances represent a limiting factor for the material ductility.

Note that in Fig. 13 we show the deformed shape in order to have a clear perception of the straining of the samples during the process of plastic localization. Thus, we point out that the development of the pair of localization bands is accompanied by a substantial reduction of the width of the sample near the localization area. As shown in Fig. 8, such kind of localization pattern with a single pair of bands inside a necked region (local width reduction) is representative of the largest samples tested. However, it does not find correlation with the experimental failure pattern observed for $V_0 = 5\ m/s$ and $L_2 = 20\ mm$, for which multiple localization bands and little width reduction near the fracture location were observed (see Fig. 8). This mismatch between the numerical calculation and the experimental counterpart is mostly attributed to the simplicity of our finite element model which only takes into account the gauge of the sample. In the experimental sample, the fillets and the gripping sections increase the momentum of inertia of the cross section (along the Y direction). We assume that this opposes to the local width reduction near the failure point, enhancing the formation of multiple necking bands. This statement is confirmed with Fig. 14, where we show contours of equivalent strain rate for model A-2 in Fig. 14(a) and model B-2 in Fig. 14(b). As for Fig. 13, the loading velocity is $V_0 = 5\ m/s$ and the sample length is $L_2 = 20\ mm$. The Eulerian (deformed shape) configuration is depicted. The localization strain corresponding to model A-2 is $\bar{\varepsilon}_l^p \approx 0.85$ while for model B-2 the specimen never reaches the condition of full localization. Thus, we have:

- Because of the difference in the initial conditions, model A-2 shows lower ductility than model B-2.
- Because of the difference in the boundary conditions, model A-2 shows larger ductility than model A-1 and model B-2 shows larger ductility than model B-1.

Since the effect of the initial conditions in the material ductility was already discussed above, we analyse here the role played by the boundary conditions. It has to be recalled that, as described in section 5, the boundary conditions applied to models A-2 and B-2 are such that all the nodes located at the surfaces $\{X, \pm\frac{W}{2}, Y\}$ have identical displacement along the Y axis during the calculation (thus impeding the local width reduction of the sample). The application of such boundary conditions, which try to emulate an infinite plate along the Y direction (see section 5), delays flow localization and promotes the emergence of multiple localization bands. These results suggest that:

- If the metallic sheet has a large slenderness L_2/W such that it mostly behaves like a rod then: (1) flow localization is promoted and (2) a single pair of necking bands contained in the $\{X, Z\}$ plane are formed inside a necked region contained in the $\{Y, Z\}$ plane.
- If the metallic sheet shows a short slenderness L_2/W such that it mostly behaves like a plate then: (1) flow localization is delayed and (2) multiple necking bands contained in the $\{X, Z\}$ plane are formed.

In order to deepen into the previous two observations, we carry out additional numerical calculations for models A-1 and A-2 in which different values of W have been explored: 2 mm, 10 mm (reference width as shown in Fig. 10), 30 mm, 40 mm, 80 mm, 140 mm, 280 mm, 560 mm and 600 mm. In order to maintain the longitudinal inertial resistance to motion of the specimen we have used for all the computations the same applied velocity $V_0 = 5\ m/s$ and sample length $L_2 = 20\ mm$. Recall that for model A-1 the surfaces $\{X, \pm\frac{W}{2}, Z\}$ are free of constrains (in such

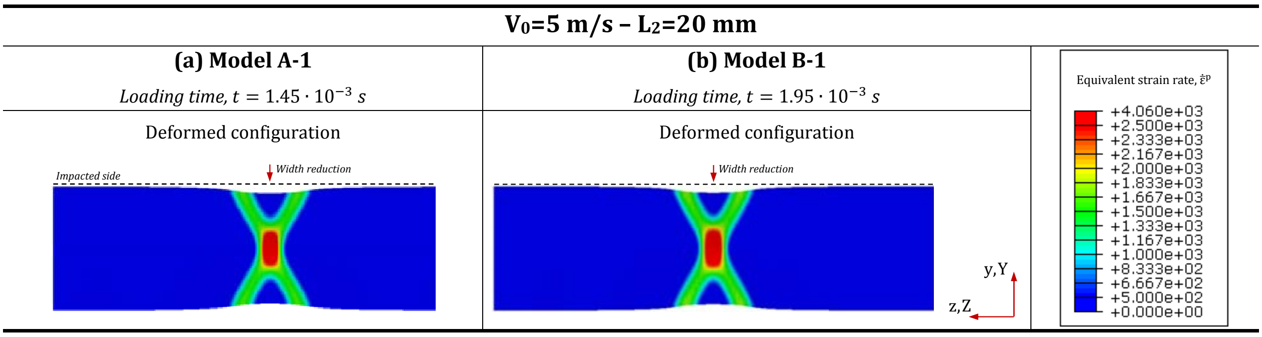

Figure 13: Finite element results. Contours of equivalent strain rate $\dot{\bar{\varepsilon}}^p$ in Eulerian (deformed shape) configuration for $V_0 = 5\ m/s$ and $L_2 = 20\ mm$. (a) Model A-1, loading time $t = 1.45 \cdot 10^{-3}\ s$. (b) Model B-1, loading time $t = 1.95 \cdot 10^{-3}\ s$.

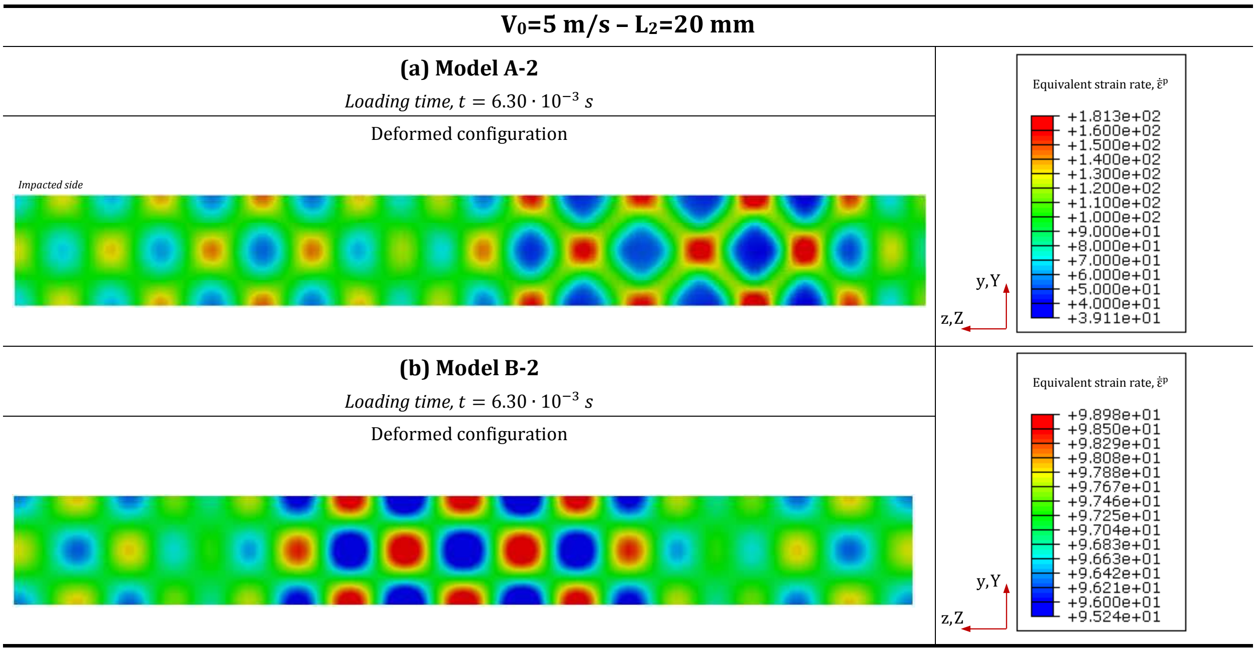

Figure 14: Finite element results. Contours of equivalent strain rate $\dot{\bar{\varepsilon}}^p$ in Eulerian (deformed shape) configuration for $V_0 = 5\ m/s$ and $L_2 = 20\ mm$. (a) Model A-2, loading time $t = 6.30 \cdot 10^{-3}\ s$. (b) Model B-2, loading time $t = 6.30 \cdot 10^{-3}\ s$.

a sense this configuration is representative of an experimental test) whereas for model A-2 all the nodes of the surfaces $\{X, \pm\frac{W}{2}, Z\}$ undergo the same displacement along the Y direction. Fig. 15 shows the localization strain $\bar{\varepsilon}_l^p$ versus the sample slenderness L_2/W.

- Model A-1: there is a significant increase of the localization strain with the decrease of sample slenderness within the greatest values of L_2/W considered. Nevertheless, the rise of $\bar{\varepsilon}_l^p$ becomes gradually reduced as L_2/W decreases, such that within the range $L_2/W < 0.1$ the localization strain tends asymptotically to ~ 0.39. We have observed that the localization pattern evolves from a single pair of bands inside a necked region for large values of L_2/W to multiple necking bands for short values of L_2/W. This interplay between the specimen slenderness and the failure pattern finds good correlation (qualitative agreement) with the experimental trends shown in Fig. 8.

  Note that irrespective of the ratio L_2/W the sample is subjected to uniaxial tension during the process of homogeneous deformation. It is only after the perturbation of the fundamental solution, within the post-uniform deformation regime (after the diffuse localization and prior to the full localization [52, 76, 77]), when samples with different aspect ratios L_2/W may behave in a different manner due to the development of stress gradients along the Y direction.

- Model A-2: the localization strain tends to infinity for the greatest values of L_2/W studied. The imposed boundary condition in the sample-surfaces $\{X, \pm\frac{W}{2}, Z\}$ does not allow to develop a necked region contained in the $\{Y, Z\}$ plane (the natural localization pattern of the samples that mostly behave like a rod, see Fig. 13) and the specimen ductility *virtually* tends to infinity. Finite values of the localization strain are found for $L_2/W < 2$. For this range of the ratio L_2/W the localization strain decreases non-linearly with the decrease of the sample slenderness. This drop becomes gradually mitigated as L_2/W decreases, such that within the range $L_2/W < 0.1$ the localization strain tends asymptotically to ~ 0.39.

  Within the range $0.1 < L_2/W < 2$ flow localization is reached but, in comparison with the model A-1, the process requires the investment of a greater amount of external work. The sample undergoes localization but, due to the imposed boundary conditions, without following the natural pattern of the specimen. For $L_2/W < 0.1$ the imposed boundary conditions do not affect the localization process, thus models A-1 and A-2 provide very similar localization strain and failure pattern. Then, the samples with aspect ratio $L_2/W < 0.1$ can be considered, for all purposes, as infinite plates. This is further illustrated in Fig. 16 where, for models A-1 and A-2, we show contours of equivalent plastic strain $\bar{\varepsilon}^p$ in the Eulerian configuration (deformed shape) for $L_2 = 20\ mm$ and $W = 280\ mm$ ($L_2/W = 0.0714$). We observe that the failure pattern is now characterized, irrespective of the model selected (either A-1 or A-2), by the emergence of multiple necking bands contained in the $\{X, Z\}$ plane.

The finite element calculations presented in this section explain the experimental observations previously reported in section 3.3, and illustrate the effect that the specimen slenderness and the boundary conditions have on the emergence of multiple localization patterns.

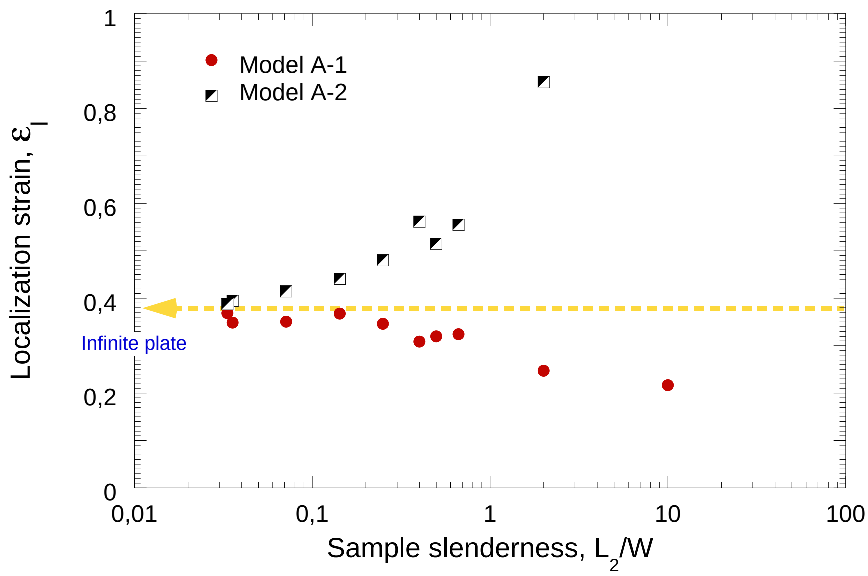

Figure 15: Finite element results. Models A-1 and A-2. Localization strain $\bar{\varepsilon}^p_l$ versus sample slenderness L_2/W.

Note that, while our simple geometrical models neglect the influences of the shoulders of the specimen as well as possible wave transmissions and reflections from/to the machine in the location of flow localization, they capture the essential features of the interplay between fracture location, loading velocity and sample size observed in the experiments.

7. Summary and conclusions

In this paper we have investigated whether the nature of the fracture location in the dynamic tensile testing of metallic sheets is deterministic or random. For that purpose we have carried out experiments and finite element simulations. The results have revealed some key mechanisms

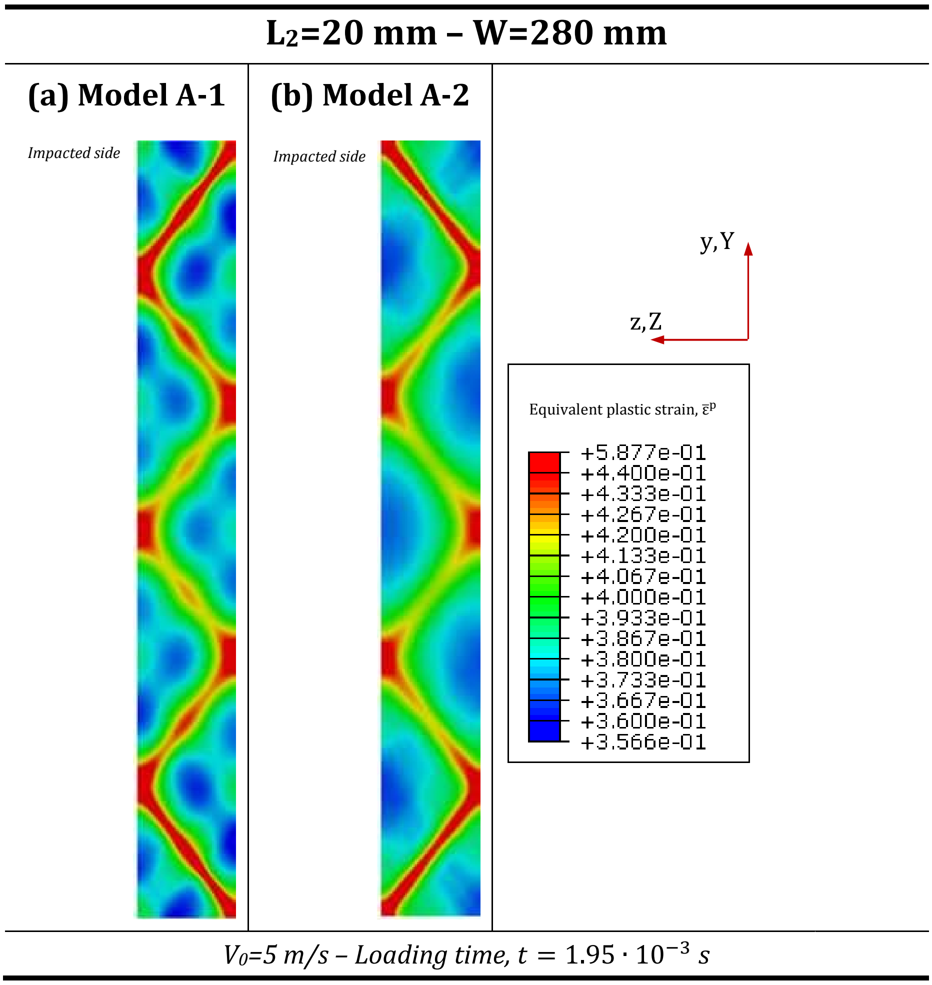

Figure 16: Finite element results. Contours of equivalent plastic strain $\bar{\varepsilon}^p$ in the Eulerian configuration (deformed shape) for $L_2 = 20\ mm$ and $W = 280\ mm$, i.e. $L_2/W = 0.0714$. Applied velocity $V_0 = 5\ m/s$, loading time $t = 1.95 \cdot 10^{-3}\ s$. (a) Model A-1. (b) Model A-2.

which play a dominant role in the development of flow localization and subsequent fracture of the specimen.

- Experiments: we have conducted a comprehensive experimental campaign in which a large number of specimens with different gauge lengths ranging from 20 mm to 140 mm have been tested at velocities varying from 1 m/s to 7.5 m/s. For each combination of gauge-length/applied-velocity we have carried out several repeats which have revealed an extremely high repeatability in the fracture location. This is a key experimental finding of this paper which shows that the fracture location is not random but deterministic.

  Moreover, we claim that the deterministic character of the fracture location is directly connected with the intervention of dynamic effects (stress waves and inertia) during the test. We further investigate this statement paying specific attention to the role played by the applied velocity and the gauge length, since these factors control to a large extent the processes of reflection and interaction of waves taking place in the sample during the test. For different impact velocities we have different magnitudes of the stress waves induced in the specimen, while for different gauge lengths the stress waves need different times to go over the gauge. Thus, we claim that the systematic motion from side to side of the sample that shows the fracture location with the variations in impact velocity and gauge length is an additional proof of the deterministic character of the strain localization process.

  Nevertheless, it is not only the failure location which depends on the applied velocity and the gauge length, but the failure pattern also does. While short samples tested at high velocities are prone to develop multiple and highly regular localization bands, large samples tested at low velocities use to develop a single pair of bands inside a necked region. We conclude that the emergence of multiple localization bands is favoured in those samples with low slenderness for which the strain field along the gauge is kept highly uniform during the loading process.

- Finite element simulations: previous experimental findings have been further explained using numerical calculations. For that purpose, to consider a simple geometrical model which solely accounts for the gauge of the sample has proven to be sufficient. Different initial and boundary conditions have been used, leading to four distinctive numerical configurations named in section 5 as models A-1, A-2, B-1 and B-2.

Model A-1, for which the initial and boundary conditions are representative of a typical experimental test, has been used to check the interplay between the location of plastic strain localization, the applied velocity and the gauge length. In qualitative agreement with the experiments, the computations predict that the location of plastic localization changes with variations in the impact velocity and the slenderness of the sample. This reinforces the idea that stress waves and inertia are main factors which control flow localization.

Moreover, the confrontation of the results obtained from models A-1, A-2, B-1 and B-2 allowed to point out two key issues. The first one refers to the increased ductility registered in the calculations for which the field variables (velocity, stress, strain and displacement) have been initialized. In agreement with different works available in the literature, we have shown that the stress waves, under specific loading conditions, may represent a limiting factor for the sample ductility. The second key issue refers to the role played by the boundary conditions in the specimen ductility and localization pattern. We have shown that the application of boundary conditions representative of an infinite plate (infinite width) to a sheet with finite width may lead to a substantial increase of the sample ductility and a strong modification of the localization pattern which (always) takes the form of multiple necking bands. From previous statement we have derived two relevant conclusions: (1) if the metallic sheet has a large slenderness such that it mostly behaves like a rod then flow localization is promoted and a single pair of necking bands contained inside a necked region are formed, (2) if the metallic sheet shows a short slenderness such that it mostly behaves like a plate then flow localization is delayed and multiple necking bands are formed. Note that previous conclusions (1) and (2) agree with our experimental findings.

All in all, in this paper we have emphasized the deterministic character of the fracture location in the dynamic tensile test. Moreover, the combination of an extensive experimental work with detailed numerical calculations has brought some insights into the key factors which control flow localization and fracture in dynamically loaded metallic sheets. Special attention has to be paid to the fact that the specimen ductility, far from being a material property, is highly dependent on the sample size, the initial conditions and the boundary conditions.

Acknowledgements

The authors are indebted to the Ministerio de Ciencia e Innovación de España (Project DPI/2011-24068) for the financial support received which allowed conducting this work.

J. A. Rodríguez-Martínez thanks J. Fernández-Sáez, A. Molinari, D. Rittel, G. Vadillo and R. Zaera for helpful discussions on dynamic necking problems.

Appendix A. Complete set of dynamic experiments

In Table A.3 we show the complete set of dynamic experiments, providing the fracture location in each case.

		Fracture location					
Velocity (m/s)	**Specimen**	**L_2 = 20 mm**	**L_2 = 40 mm**	**L_2 = 60 mm**	**L_2 = 80 mm**	**L_2 = 100 mm**	**L_2 = 140 mm**
1	**1**	*Centre*	*Impact*	*Impact*	*Impact*	*Clamped*	*Clamped*
	2	*Centre*	*Impact*	*Impact*	*Clamped*	*Clamped*	*Clamped*
	3	*Centre*	*Impact*	*Impact*	*Clamped*	*Clamped*	*Clamped*
	4	*N/A*	*N/A*	*N/A*	*Clamped*	*N/A*	*N/A*
1,75	**1**	*Centre*	*Impact*	*Clamped*	*Impact*	*Impact*	*Centre*
	2	*Centre*	*Impact*	*Clamped*	*Impact*	*Impact*	*Centre*
	3	*Centre*	*Clamped*	*Clamped*	*Impact*	*Impact*	*Centre*
	4	*N/A*	*Impact*	*N/A*	*N/A*	*N/A*	*N/A*
2,5	**1**	*Centre*	*Impact*	*Impact*	*Impact*	*Clamped*	*Centre*
	2	*Centre*	*Impact*	*Clamped*	*Clamped*	*Clamped*	*Centre*
	3	*Centre*	*Impact*	*Clamped*	*Clamped*	*Clamped*	*Centre*
	4	*Centre*	*N/A*	*Clamped*	*Clamped*	*N/A*	*N/A*
3,75	**1**	*Centre*	*Impact*	*Clamped*	*Clamped*	*Impact*	*Clamped*
	2	*Centre*	*Impact*	*Clamped*	*Centre*	*Impact*	*Impact*
	3	*Centre*	*Impact*	*Clamped*	*Clamped*	*Impact*	*Clamped*
	4	*N/A*	*N/A*	*Clamped*	*Clamped*	*N/A*	*Clamped*
5	**1**	*Centre*	*Impact*	*Clamped*	*Clamped*	*Clamped*	*Centre*
	2	*Centre*	*Impact*	*Clamped*	*Clamped*	*Clamped*	*Clamped*
	3	*Centre*	*Impact*	*Clamped*	*Clamped*	*Clamped*	*Centre*
	4	*N/A*	*N/A*	*N/A*	*N/A*	*N/A*	*Centre*
6,25	**1**	*Centre*	*Impact*	*Clamped*	*Clamped*	*Impact*	*Clamped*
	2	*Centre*	*Impact*	*Clamped*	*Clamped*	*Clamped*	*Clamped*
	3	*Centre*	*Impact*	*Clamped*	*Clamped*	*Impact*	*Clamped*
	4	*Centre*	*N/A*	*N/A*	*N/A*	*Impact*	*N/A*
7,5	**1**	*Centre*	*Impact*	*Impact*	*Clamped*	*Impact*	*Clamped*
	2	*Centre*	*Impact*	*Impact*	*Clamped*	*Clamped*	*Clamped*
	3	*Centre*	*Impact*	*Impact*	*Clamped*	*Clamped*	*Clamped*
	4	*N/A*	*N/A*	*N/A*	*N/A*	*Clamped*	*N/A*

Table A.3: *Complete set of dynamic experiments. For each test we indicate the fracture location.*

Appendix B. Mesh sensitivity analysis

In order to check the mesh independence of our numerical calculations we have carried out computations using three different mesh densities:

- Mesh 1: the elements dimensions are $0.166 \times 0.333 \times 0.166\ mm^3$ (reference configuration).
- Mesh 2: the elements dimensions are $0.125 \times 0.250 \times 0.125\ mm^3$.
- Mesh 3: the elements dimensions are $0.100 \times 0.200 \times 0.100\ mm^3$.

Fig. B.17. shows finite elements results obtained using these three mesh densities for the model A-1, the loading velocity $V_0 = 5\ m/s$ and the gauge length $L_2 = 20\ mm$. We illustrate the equivalent plastic strain $\bar{\varepsilon}^p$ versus the normalized specimen coordinate $\bar{Z} = \dfrac{z}{L_2}$ for the loading time $t = 1.45 \cdot 10^{-3}\ s$. The excursions of strain represent the necking bands. The results corresponding to the three different mesh densities practically overlap to each other, which confirms that our computations are largely insensitive to the mesh size. Therefore, in order to have the smallest computational time, the coarser mesh (Mesh 1) was used in all the numerical simulations shown in this paper.

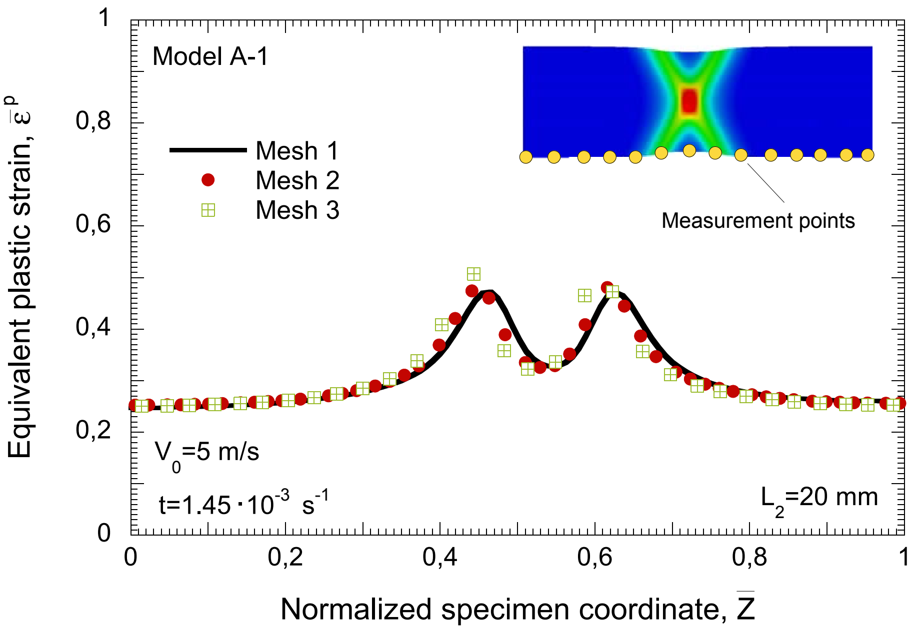

Figure B.17: Finite element results. Model A-1. Equivalent plastic strain $\bar{\varepsilon}^p$ versus the normalized specimen coordinate $\bar{Z} = \dfrac{z}{L_2}$. Gauge length $L_2 = 20\ mm$. Impact velocity $V_0 = 5\ m/s$. Loading time $t = 1.45 \cdot 10^{-3}\ s$. Results are shown for mesh 1, mesh 2 and mesh 3.

References

[1] Nadai A, Manjoine MJ. High-speed tension tests at elevated temperatures. Parts II and III. Journal of Applied Mechanics 1941;63:A–77, A–91.

[2] De Forest AV, MacGregor CW, Anderson AR. Rapid Tension Tests Using the Two-Load Method; chap. Institute of Metals Division (In Metals Technology). American Institute of Mining and Metallurgical Engineers; 1941, p. 1–9.

[3] Clark DS. The Infiuence of Impact Velocity on the Tensile Characteristics of Some Aircraft Metals and Alloys. Tech. Rep.; Nationa1 Advisory Committee for Aeronautics; 1942.

[4] Parker E, Ferguson C. The effect of strain rate upon the tensile impact strength of some metals. Transactions of the American Society for Metals 1942;30:68–80.

[5] Manjoine M. Influence of rate of strain and temperature on yield stress of mild steel. Journal of Applied Mechanics Transactions of the ASME 1944;11:211–8.

[6] Mann HC. High-velocity tension-impact tests. Proceedings–American Society of Testing Materials 1936;36:85–109.

[7] Mann HC. Fundamental study of the design of impact test specimens. Proceedings–American Society of Testing Materials 1937;37:102–30.

[8] Clark DS, Datwyler G. Stress–strain relations under tension impact loading. Proceedings–American Society of Testing Materials 1938;38:98–111.

[9] Beardsley GF, Coates LD. A study of the effect of repeated tension impact loads upon certain metals used in aircraft construction. Master's thesis; California Institute of Technology; 1939.

[10] Genter WEJ, Biglow JO. A study of the effect of repeated tension impact loads upon certain metals used in aircraft construction. Master's thesis; California Institute of Technology; 1940.

[11] Olsen CB, Brown SW. A study of the effect of repeated tension impact loads upon certain metals used in aircraft construction. Master's thesis; California Institute of Technology; 1942.

[12] Duwez PE, Clark PE. An experimental study of the propagation of plastic deformation under conditions of longitudinal impact. Proceedings–American Society of Testing Materials 1947;47:502–32.

[13] Clark PE, Duwez PE. Discussion of the forces acting in tension impact test of materials. Journal of Applied Mechanics 1948;15:243–7.

[14] Clark PE, Duwez PE. The influence of strain rate of some tensile properties of steel. Proceedings of the American Society for Testing Materials 1950;:560–75.

[15] Clark PE, Wood DS. The tensile impact properties of some metals and alloys transactions. American Society of Metals 1950;42:45–74.

[16] Von Kármán T. On the propagation of plastic deformation in solids. Tech. Rep.; National Defense Research Committee. Office of Scientific Research and Development N 365; 1942.

[17] Rakhmatulin KA. Mechanics of unloading waves. Prikladnaya Matematika i Mekhanika 1945;9:191–00.

[18] Taylor GI. The Testing of aterials at High Rates of Loading. Journal of the Institution of Civil Engineers 1946;26:486–519.

[19] White MP, Griffis L. The permanent strain in a uniform bar due to longitudinal impact. Journal of Applied Mechanics 1947;14:337–43.

[20] Malvern LE. Plastic Wave Propagation in a Bar of Material Exhibiting a Strain Rate Effect. Quarterly of Applied Mathematics 1951;8:405–11.

[21] Harding J, Wood EO, Campbell JD. Tensile Testing of Materials at Impact Rates of Strain. Journal of Mechanical Engineering Science 1960;2:488–96.

[22] Simmons SA, Hauserf E, Dorn J. Response of Metals to High Velocity Deformation. Interscience; 1961, p. 1–14.

[23] Lindholm US. Some experiments with the Split Hopkinson Pressure bar. Journal of the Mechanics and Physics of Solids 1964;12:317–35.

[24] Nicholas T. Mechanical Properties of Structural Grades of Beryllium at High Strain Rates. Tech. Rep.; Air Force Materials Laboratory; 1975.

[25] Nicholas T. Dynamic Tensile Testing of Structural Materials Using a Split Hopkinson Bar Apparatus. Tech. Rep.; Air Force Wright Aeronautical Laboratories; 1980.

[26] Nicholas T. Tensile testing of materials at high rates of strain. Experimental Mechanics 1981;21:177–85.

[27] Lubliner J. A generalized theory of strain-rate-dependent plastic wave propagation in bars. Journal of the Mechanics and Physics of Solids 1964;12:59–65.

[28] Botte R, Rousseau T, Peguin P, Gobin P. Calculation of the behaviour of a bar during a high-strain-rate tensile test. Journal of Physics D: Applied Physics 1967;18:663–70.

[29] Botte R, Rousseau T, Gobin P. A theoretical and experimental analysis of high strain-rate test using Malverns̀ theory. Journal of Physics D: Applied Physics 1969;2:1235–43.

[30] Matic P, Kirby III GC, Jolles MI. The relation of tensile specimen size and geometry effects to unique constitutive parameters for ductile materials. Proceedings of the Royal Society of London Series A, Mathematical and Physical Sciences 1988;417:309–33.

[31] Nemes JA, Eftis J. Constitutive modelling on the dynamic fracture of smooth tensile bars. International Journal of Plasticity 1993;9:243–70.

[32] Glema A, Lodygowski T, Perzyna P. Interaction of deformation waves and localization phenomena in inelastic solids. Computers Methods in Applied Mechanics and Engineering 2000;183:123–40.

[33] Rusinek A, Cheriguene R, Baümer P, Klepaczko JR, Larour P. Dynamic behaviour of high-strength sheet steel in dynamic tension: experimental and numerical analyses. Journal of Strain Analysis for Engineering Design 2008;43:37–43.

[34] Huh H, Kim SB, Song JH, Lim JH. Dynamic tensile characteristics of TRIP-type and DP-type steel sheets for an auto-body. International Journal of Mechanical Sciences 2008;50:918–31.

[35] Mirone G. The dynamic effect of necking in Hopkinson bar tension tests. Mechanics of Materials 2013;58:84–96.

[36] Rusinek A, Zaera R, Klepaczko JR, Cheriguene R. Analysis of inertia and scale effects on dynamic neck formation during tension of sheet steel. Acta Materialia 2005;53:5387–400.

[37] Wood WW. Experimental mechanics at velocity extremes-very high strain rates. Experimental Mechanics 1965;5:361–71.

[38] Besnard G, Hild F, Lagrange JM, Martinuzzi P, Roux S. Analysis of necking in high speed experiments by stereocorrelation. International Journal of Impact Engineering 2012;49:179–91.

[39] Osovski S, Rittel D, Rodríguez-Martínez JA, Zaera R. Dynamic tensile necking: Influence of specimen geometry and boundary conditions. Mechanics of Materials 2013;62:1–13.

[40] Rittel D, Rotbaum Y, Rodríguez-Martínez JA, Sory D, Zaera R. Dynamic Necking of Notched Tensile Bars: An Experimental Study. Experimental Mechanics 2014;54:1099–109.

[41] Simulia . ABAQUS/Explicit User's Manual. Providence, USA: Dassault Systèmes; version 6.10 ed.; 2010.

[42] AK steel corporation. Product Data Sheet. 430 stainless steel. 9227 Centre Pointe Drive. West Chester, OH 45069; 2007.

[43] Rodríguez-Martínez JA, Pesci R, Rusinek A. Experimental study on the martensitic transformation in AISI 304 steel sheets subjected to tension under wide ranges of strain rate at room temperature. Materials Science and Engineering: A 2011;528:5974–82.

[44] Mansur MA, Wee TH, Chin MS. Derivation of the complete stress-strain curves for concrete in compression. Magazine of Concrete Research 1995;47:285–90.

[45] Battams G. The Use of Optical Techniques to Assess the Damage Tolerance of composite Materials. Ph.D. thesis; University of Southampton, United Kingdom; 2014.

[46] Rodríguez-Martínez JA, Rittel D, Zaera R, Osovski S. Finite element analysis of AISI 304 steel sheets subjected to dynamic tension: the effects of martensitic transformation and plastic strain development on flow localization. International Journal of Impact Engineering 2013;53:206–16.

[47] Storen S, Rice J. Localized necking in thin sheets. Journal of the Mechanics and Physics of Solids 1975;23:421–41.

[48] Zhang H, Ravi-Chandar K. On the dynamics of necking and fragmentation - II. Effect of material properties geometrical constraints and absolute size. International Journal of Fracture 2008;150:3–36.

[49] Rotbaum Y, Osovski S, Rittel D. Why does necking ignore notches in dynamic tension ? Experimental Mechanics 2015;78:173–85.

[50] Rodríguez-Martínez JA, Rusinek A, Arias A. Relation between strain hardening of steel and critical impact velocity. Journal of Theoretical and Applied Mechanics 2009;47:645–65.

[51] Fressengeas C, Molinari A. Fragmentation of rapidly stretching sheets. European Journal of Mechanics A/Solids 1994;13:251–68.

[52] Rodríguez-Martínez JA, Vadillo G, Fernández-Sáez J, Molinari A. Identification of the critical wavelength responsible for the fragmentation of ductile rings expanding at very high strain rates. Journal of the Mechanics and Physics of Solids 2013;61:1357–76.

[53] Altynova M, Hu X, Daehn GS. Increased ductility in high velocity electromagnetic ring expansion. Metall Trans A 1996;27:1837–44.

[54] Grady DE, Olsen ML. A statistics and energy based theory of dynamic fragmentation. International Journal of Impact Engineering 2003;29:293–306.

[55] Hiroe T, Fujiwara K, Hata H, Takahashi H. Deformation and fragmentation behaviour of exploded metal cylinders and the effects of wall materials, configuration,explosive energy and initiated locations. International Journal of Impact Engineering 2008;35:1578–86.

[56] Goto D, Becker R, Orzechowski T, Springer H, Sunwoo A, Syn C. Investigation of the fracture and fragmentation of explosively driven rings and cylinders. International Journal of Impact Engineering 2008;35:1547–56.

[57] Mercier S, Granier N, Molinari A, Llorca F, Buy F. Multiple necking during the dynamic expansion of hemispherical metallic shells, from experiments to modelling. Journal of the Mechanics and Physics of Solids 2010;58:955–82.

[58] Mercier S, Molinari A. Predictions of bifurcations and instabilities during dynamic extensions. International Journal of Solids and Structures 2003;40:1995–2016.

[59] Zaera R, Rodríguez-Martínez JA, Vadillo G, Fernández-Sáez J. Dynamic necking in materials with strain induced martensitic transformation. Journal of the Mechanics and Physics of Solids 2014;64:316–37.

[60] Klepaczko JR. Introduction to Experimental Techniques for Material Testing at High Strain Rates. Scientific Library. Warszawa Institute of Aviation; 2007.

[61] Nemat-Nasser S, Guo W. High strain-rate response of commercially pure vanadium. Mechanics of Materials 2000;32:243–60.

[62] Rusinek A, Klepaczko JR. Shear testing of a sheet steel at wide range of strain rates and a constitutive relation with strain-rate and temperature dependence of the flow stress. International Journal of Plasticity 2001;17:87–115.

[63] Xue Z, Vaziri A, Hutchinson JW. Material aspects of dynamic neck retardation. Journal of the Mechanics and Physics of Solids 2008;56:93–113.

[64] Needleman A. The effect of material inertia on neck development. Topics in Plasticity; Ann Arbor, MI: AM Press; 1991, p. 151–60.

[65] Rusinek A, Zaera R. Finite element simulation of steel ring fragmentation under radial expansion. International Journal of Impact Engineering 2007;34:799–822.

[66] Zukas JA, Scheffer DR. Practical aspects of numerical simulations of dynamic events: effects of meshing. International Journal of Impact Engineering 2000;24:925–45.

[67] Needleman A. Material rate dependence and mesh sensitivity in localization problems. Computer Methods in Applied Mechanics and Engineering 2008;67:69–85.

[68] Molinari A. Collective behaviour and spacing of adiabatic shear bands. Journal of the Mechanics and Physics of Solids 1997;45:1551–75.

[69] Zaera R, Fernández-Sáez J. An implicit consistent algorithm for the integration of thermoviscoplastic constitutive equations in adiabatic conditions and finite deformations. International Journal of Solids and Structures 2006;43:1594–612.

[70] Simó JC, Hughes TJR. Computational Inelasticity. New York: Springer; 1998.

[71] Doghri I. Mechanics of deformable solids: linear and nonlinear, analytical and computational aspects. Berlin: Springer; 2000.

[72] Klepaczko JR. Review on critical impact velocities in tension and shear. International Journal of Impact Engineering 2005;32:188–209.

[73] Zaera R, Rodríguez-Martínez JA, Vadillo G, Fernández-Sáez J, Molinari A. Collective behaviour and spacing of necks in ductile plates subjected to dynamic biaxial loading. Journal of the Mechanics and Physics of Solids 2015;Submitted for Publication.

[74] Triantafyllidis N, Waldenmyer JR. Onset of necking in electro-magnetically formed rings. Journal of the Mechanics and Physics of Solids 2004;52:2127–48.

[75] Hu X, Daehn GS. Effect of velocity on flow localization in tension. Acta Materialia 1996;44:1021–33.

[76] Zhou F, Molinari JF, Ramesh KT. An elasto-visco-plastic analysis of ductile expanding ring. Int J Impact Eng 2006;33:880–91.

[77] Vadillo G, Rodríguez-Martínez JA, Fernández-Sáez J. On the interplay between strain rate and strain rate sensitivity on flow localization in the dynamic expansion of ductile rings. International Journal of Solids and Structures 2012;49:481–91.